CFDシミュレーションによる潮流発電装置増速器の最適化

浦川, 皐一郎
九州大学大学院総合理工学府大気海洋環境システム学専攻

平成 30 年度

九州大学大学院総合理工学府

大気海洋環境システム学専攻修士論文

A Numerical Study on the Performance of Diffuser for a New Tidal Turbine

CFD シミュレーションによる
潮流発電装置増速器の最適化

氏名：浦川　皐一郎

指導教員：胡　長洪　教授

Abstract

Tidal current energy is one of the most important ocean renewable energies, which can be utilized by a tidal current turbine. Comparing with solar power generation and wind power generation, the power output by tidal power generation is predictable because the tidal current is periodic and is not affected by the weather. Conventional tidal current turbine has the problem of high installing and maintenance cost because it is installed at bottom of the sea. This is one of the biggest obstacles in implementation of the tidal current power generation. To solve the high cost problem, a new tidal power generation concept, the floating type diffuser augmented tidal current turbine, has been proposed and a feasibility study on this new concept has been carried out (Obara, 2017) in our laboratory. In this study, as a continuation of the previous research, I focus on optimization of the diffuser shape. Particularly I want to find the influence of the diffuser thickness on the flow velocity increase inside the diffuser and the drag force on the diffuser by using CFD simulation. OpenFOAM is used for the numerical simulation. Three diffuser models with different thickness are considered. Numerical simulations are performed on the three diffuser models without turbine under different inflow velocities. The results of velocity distribution, drag coefficient, streamline, vorticity and pressure distribution are compared among the three diffuser models and the effect of diffuser thickness on the performance of the tidal current turbine is discussed. Finally, a numerical simulation on a diffuser augmented turbine model is carried out to examine the effect of the turbine rotation.

Key words

Table of Contents

Chapter 1: Introduction

1.1. Background

1.1.1. World Energy Situation

Today, worldwide population growth is proceeding, and energy demand is rapidly increasing. Due to environmental concerns, a movement to use renewable energy is spreading mainly in developed countries. According to the United Nations, the world population, which was about 6.1 billion[1] people in 2000, is currently 7.3 billion[1] people. By 2040, It is expected to exceed 9 billion[1] people. The concentration of the population is also a major issue. In 2015, the combined population of China and India was about 2.7 billion[1], accounting for about 38% of the world. It is expected that the population of India and Africa will further increase in the future. In response to this population increase, energy demand in the world is expected to increase. Since there are regions where extreme energy shortage is occurring, energy supply is a major problem of humankind. Fig. 1-1[2] shows the global energy demand which changes from 2016 to 2040. The highest increase is in India, followed by China. Energy demand will increase in many parts of the world. On the other hand, it is expected that it will decrease in advanced countries with a high interest in the environment. Especially in Europe, it is expected to decrease by 200 Mtoe[2].
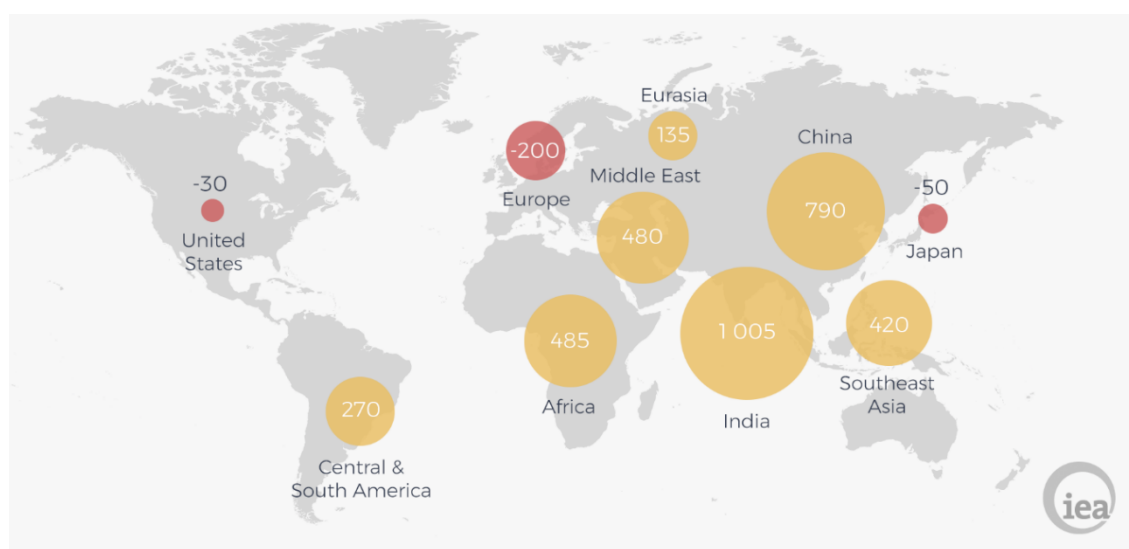
Fig. 1-1 Change in primary energy demand, 2016-40 (Mtoe)[1]

1.1.2. Energy situation in Japan

Self-sufficiency ratio in the primary energy supply of Japan is quite low. Therefore, most of the fossil fuels, which are used in power generation, are imported from overseas, especially middle east Asia. Since fossil fuels have biases in countries and regions where they are produced, relying on a single resource is a significant risk. One famous example is the first oil shock in the 1970s. In 1973, when the oil shock occurred, the ratio of petroleum in Japan's energy reached 75.5%[3]. Therefore, the Japanese economy suffered severe damage from rising oil prices. That is the reason why the Japanese government promoted the use of nuclear energy, natural gas, coal, et cetera. as substitute energy sources for oil with the goal for stabilizing energy supply. In particular, nuclear power generation was actively used as an important power supply because it can stably obtain relatively large energy. As a result, the share of oil in energy decreased to 40% [3] in 2010. It was deemed that the attempt to stabilize the energy supply was successful.

However, due to the Great East Japan Earthquake on March 11, 2011, and following the Fukushima Daiichi Nuclear disaster, the Japanese government decided to reconsider the energy policies. All nuclear power plants in Japan have stopped for a long time, and the energy supply had to rely on fossil fuels such as coal, oil and natural gas. In order to compensate for the shortage of nuclear power generation, the ratio of thermal power generation in total power generation was drastically increased to 88% [4] in 2013. As a result, the procurement cost of fossil fuels is increased, and Japan has become a trade deficit country in 2011. One of the reasons for this result is an upward trend in the price of fossil fuels. As stated above, there are biases in fossil fuels abundant region, and it is expected that the situation will become more difficult to achieve stable imports in the future. Also, as dependency on thermal power generation increases, efforts to reduce greenhouse gas emission will be recessed which is one of the most severe problems.

Renewable energy is attracting attention recently as clean energy that can solve these problems. In the next section, we provide detailed explanations.

1.2. Nuclear energy vs. renewable energy

The energy crisis by the exhaustion of fossil fuels has to be avoided. The alternative energy sources for power generation are rapidly developed, in which clean energies have attracted much attention.

1.2.1. Nuclear energy

Nuclear power generation is one of the alternative energies taking advantage of nuclear power. The method to produce power in the almost contemporary nuclear power plant is that heat energy made by nuclear fission produces high-pressure steam at first and generator joined a steam turbine are rotated for electricity generation. The advantages of using nuclear energy are producing stable and massive electricity, economic due to its low cost in power generation. Nuclear energy has become a proof for high national technological strength if there is no accident, not producing greenhouse gas and exhausting oxides, which result in acid rain and photochemical smog. However, this energy has the potential dangerousness like the Fukushima Daiichi nuclear power plant accident on 11 March 2011. After this disaster, risks associated with the safety were brought to the fore [4]. Therefore, the expansion of nuclear energy will slow down.

1.2.2. Renewable energies

The renewable energy is defined as the following by International Energy Agency.

Renewable energy is derived from natural processes that are continuously replenished. In its various forms, it derives directly from the sun, or from heat generated deep within the earth. Included in the definition is electricity and heat generated from solar, wind, ocean, hydropower, biomass, geothermal resources, and biofuels and hydrogen derived from renewable resources.

The renewable energies defined above. It can replace conventional fuels in four district areas which are electricity generation, hot water or space heating and motor fuels. Renewable energy resources exist all over the world, in contrast to other energy sources like the oil which are concentrated in some limited countries. Rapid deployment of renewable energy and energy efficiency is resulting in significant energy security, climate change mitigation, and economic benefits[6]. In international public opinion surveys, there is strong support for promoting renewable sources such as solar power and wind power[7]. While many renewable energy projects are large-scale, renewable technologies are also suited to developing countries, where energy is often crucial in human development[8].

1.3. Tidal current energy

1.3.1. Principle

Tidal current power generation is the same principle as wind power generation, converts the kinetic energy of the fluid (seawater in the case of tidal current power generation, the air in case of wind power generation) into rotational energy, turning the turbine to generate electricity.

Firstly, a principle of the tide is explained. Tide is the upward and downward motion of the sea surface caused by the attraction of the moon or the sun and the sea water on the surface of the earth is attracted and repelled. In other words, the tide at a certain point is determined by the positional relationship between the point and the sun and moon. Since the earth rotates once a day, the high tide and low tide will be repeated twice a day. Besides, since the moon revolves around the earth with a period of about one month, the time between the high tide and low tide is delayed several minutes every day.

When the earth, moon, and the sun line up in line (full moon period), the tide of the moon and the tidal force (tidal power) caused by the sun overlap, so the difference between the high tide and the low tide at that day becomes large. This period is called a flood tide. Conversely, when the moon and the sun are displaced in a perpendicular direction, the tidal difference between the high tide and the low tide becomes small, and it is called a neap tide. The flow in the horizontal direction accompanying the tidal fluctuation of the tide is called a tidal current. Since there is a cycle in the tide, the speed and direction of tide current change periodically. This means that it is relatively easy to predict the amount of power generation, which is one of the significant advantages of tidal power generation.

Next, the principle of tidal power generation is introduced by using equations.

Tidal current energy can be obtained by taking out the kinetic energy of seawater passing through the projected area. The density of seawater is defined by ρ[kg/m^2] and the current velocity defined by U [m/s]. The kinetic energy per unit time K passing through the projected area A [m^2] is given by the following equation.

$$K = \frac{1}{2}mU^2 = \frac{1}{2}(\rho AU)U^2 = \frac{1}{2}\rho AU^3 \qquad (1.1)$$

From the above equation, the kinetic energy of the tidal current is proportional to the sea water density, projected area and the cube of flow velocity. However, we cannot extract all kinetic energy of tide current.
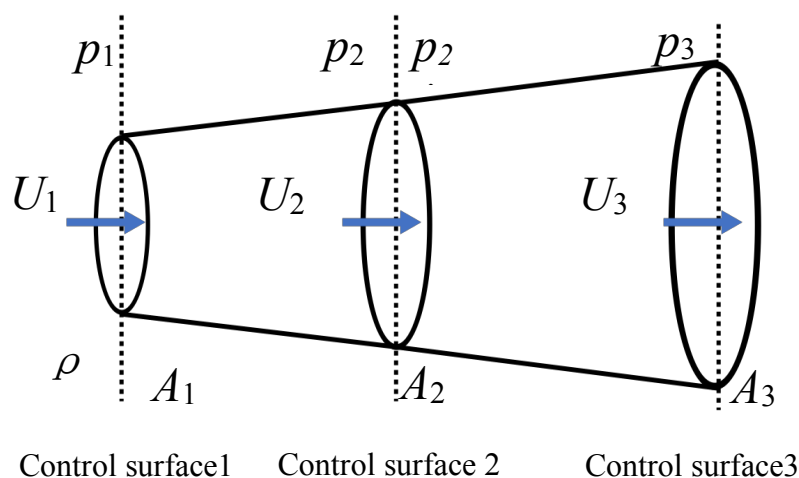

Fig.1-2 The momentum theory

Next, power generation efficiency is explained using the momentum theory.

As shown in Fig.1-2, the control surface 1 is defined as a surface in front of the turbine, the control surface 2 is defined as a surface passing through the center of the turbine, and the control surface 3 is defined as a surface behind the turbine shown in Fig.1-2. Tidal current is regarded as a steady flow. The velocity is defined as U_1 [m/s], U_2 [m/s], U_3 [m/s], at each control area. Sectional areas of the control area 1, 2 and 3 are defined as $A_1[m^2]$, $A_2[m^2]$ and A_2 [m^2]. The pressure at the control area 1 and 3 is defined as p_1 [Pa], p_3[Pa]. The pressure in front of the control area 2 and behind the control surface is p_2 [Pa], p'_2 [Pa]. When Bernoulli's theorem is applied between the control area 1 and 2, and between 2 and 3, we have.

$$p_1 + \frac{1}{2}\rho U_1{}^2 = p_2 + \frac{1}{2}\rho U_2{}^2 \tag{1.1}$$

$$p_1 + \frac{1}{2}\rho U_3{}^2 = p'_2 + \frac{1}{2}\rho U_2{}^2 \tag{1.2}$$

The water pressure difference before and after the control surface 2 is as follows.

$$p_2 - p'_2 = \frac{1}{2}\rho(U_1{}^2 - U_3{}^2) \tag{1.3}$$

This water pressure difference causes the force acting on the turbine F [N] which is shown as follows.

$$F = A_2 \times (p_2 - p'_2) = A_2 \times \frac{1}{2}\rho(U_1{}^2 - U_3{}^2) \tag{1.4}$$

The following equation holds from the equation of continuity.

$$Q = \rho A_1 U_1 = \rho A_2 U_2 = \rho A_3 U_3 \tag{1.5}$$

Eq. 1.7 is held because changes in momentum per unit time equal to the force F [N] acting on the turbine.

$$\begin{aligned} F &= (QU_1) - (QU_3) \\ &= Q(U_1 - U_3) \\ &= \rho A_2 U_2(U_1 - U_3) \end{aligned} \tag{1.6}$$

From Eq. 1.7 and 1.8 the following equation is held.

$$U_2 = \frac{U_1 + U_3}{2} \tag{1.7}$$

The power of turbine W [J/s] is as shown Eq. 1.9
The power of turbine W [J/s] is as shown Eq. 1.9

$$\begin{aligned} W &= F \times U_2 \\ \\ &= \frac{1}{2}\rho A_2(U_1{}^2 - U_3{}^2) \times \frac{U_1 + U_3}{2} \\ &= \frac{\rho A_2}{4}(U_1 + U_3)^2(U_1 - U_3) \\ &= \frac{\rho A_2 U_1{}^3}{4}\left(1 + \frac{U_3}{U_1}\right)^2\left(1 - \frac{U_3}{U_1}\right) \\ &= \frac{\rho A_2 U_1{}^3}{2} \times \frac{1}{2}(1 + \alpha)^2(1 - \alpha) \end{aligned} \tag{1.8}$$

The power of the turbine is a function of the reduction ratio α ($= U_3 / U_1$).

Theoretical efficiency is defined as η.

$$\eta = \frac{1}{2}(1 + \alpha)^2(1 - \alpha) \tag{1.9}$$

$$\frac{\partial \eta}{\partial \alpha} = \frac{1}{2}(1 + \alpha)(1 - 3\alpha) \tag{1.10}$$

From this equation, it can be found that the maximal value of W is obtained at $\alpha = 1/3$.

Therefore, the maximum power $W_{\max}$ of the turbine is expressed by the following equation.

$$W_{max} = \frac{\rho A_2 U_1{}^3}{2} \times \frac{1}{2}\left(1 + \frac{1}{3}\right)^2 \left(1 - \frac{1}{3}\right)$$

$$= 0.593 \times \frac{\rho A_2 U_1{}^3}{2} \tag{1.11}$$

From Eq. 1.12, the maximum efficiency is 59.3% when the flow velocity after passing through the turbine is 1/3 of the flow velocity in front of the turbine. This value is the limit of the power output of the turbine. It is called Betz' law. Based on the above discussion, the power P_e that can be extracted from the tidal current by the turbine is given by the following equation. $C_p\,(\leqq 0.593)$ is the power coefficient.

$$P_e = C_p \frac{1}{2}\rho A_2 U_1{}^3 \tag{1.12}$$

1.3.2. The advantages of tidal current power generation

The principle of tidal current power generation is almost the same as that of wind power generation, but the advantage of tidal current power generation is its high energy density. As stated above, the kinetic energy of the fluid is proportional to the density. Since the density of the seawater is about 800 times larger than that of the air, even at the same flow velocity the kinetic energy of the tidal current is 800 times larger than that of the wind. That is an enormous quantity. Furthermore, as stated above, since the tidal current is a periodical flow and weather does not give the effect to a tidal current turbine, it is relatively easy to predict the amount of power generation. This point contributes to the stability of power generation. Also, Japan is surrounded by the ocean, with the adjacent zones and exclusive economic zones the area is about 4,470,000 km^2 [9]. It is one of the world's leading maritime nations. In other words, Japan is very blessed with marine energy.

In summary, the advantages of tidal current power generation are mainly the following three points.

- Energy density is higher than wind power generation
- It is relatively easy to predict the amount of power generation
- Considerable potential of tidal current energy around Japan.

1.4. Tidal current turbine

1.4.1. Conventional tidal current turbine

Today, a popular type of tidal turbine is the bottom mounted tidal turbine as shown in Fig. 1-4. This conventional tidal turbine has been developed for a long time. In Goto island, a demonstration experiment is carrying out. However, the conventional tidal current turbine has not yet put into use because it has some serious problem. The biggest problem is about the cost. Both initial cost and maintenance cost is high for the conventional tidal current turbine. Since conventional tidal current turbine is installed at the bottom of the sea, special crane ships are needed when the turbine is installed and maintained.

Fig. 1-3 Conventional tidal current turbine [10]

1.4.2. New tidal current turbine [11]

In our laboratory, a new tidal power generation concept have been proposed to solve the high-cost problem and increase power generation efficiency, the floating type tidal power generation device as shown in Fig. 1-5. This new tidal turbine has three significant features.

The first feature is the diffuser, which is similar to the Wind lens, to increase the current speed across the turbine. Wind lens technology is developed by Prof. Ohya in Kyushu University, which aims at increasing efficiency of wind power generation. The details of Wind lens technology will be explained in 1.4.3. This point is essential in the case we use this new tidal current turbine because the current flow velocity is slower than around Europe. The diffuser is also used as a buoyancy body. The new tidal current turbine floats by itself when tidal current stop. It is easy to do maintenance. When heavy service performed, a ship can tow the tidal current turbine into port.

The second point is that the turbine direction is rotated automatically by a balance among gravity, buoyancy, current force and mooring force. Therefore, this new tidal current turbine can generate power using both flow directions to increase power generation efficiency.

The third point is the mooring system. It can stabilize the device using a middle anchor. Usually, as the current flow increases, there is a danger that the diffuser touches on the bottom of the sea due to a strong drawing force via the mooring system. However, the new mooring system can be designed to retard reaching the bottom and keep the device state by the middle anchor.
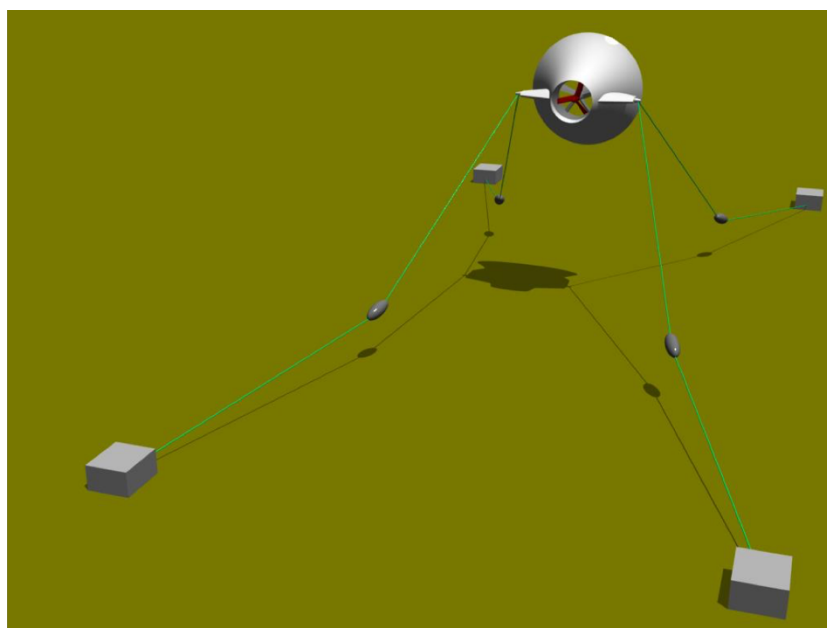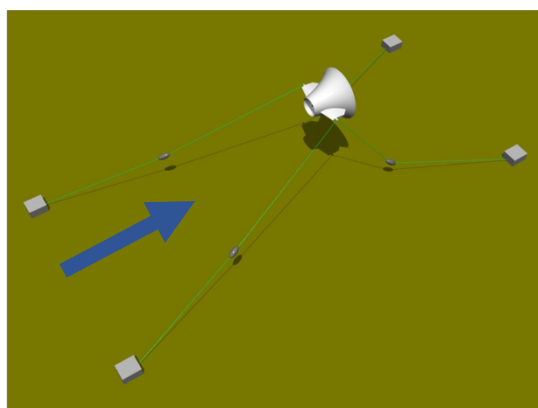

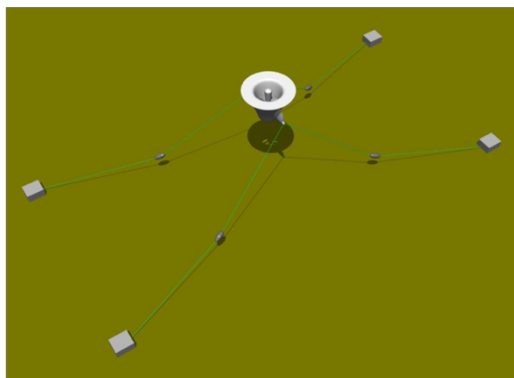Fig. 1-5 New tidal current turbine

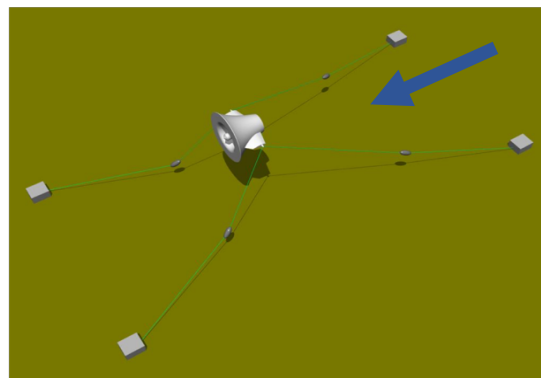Fig. 1-6 Following current
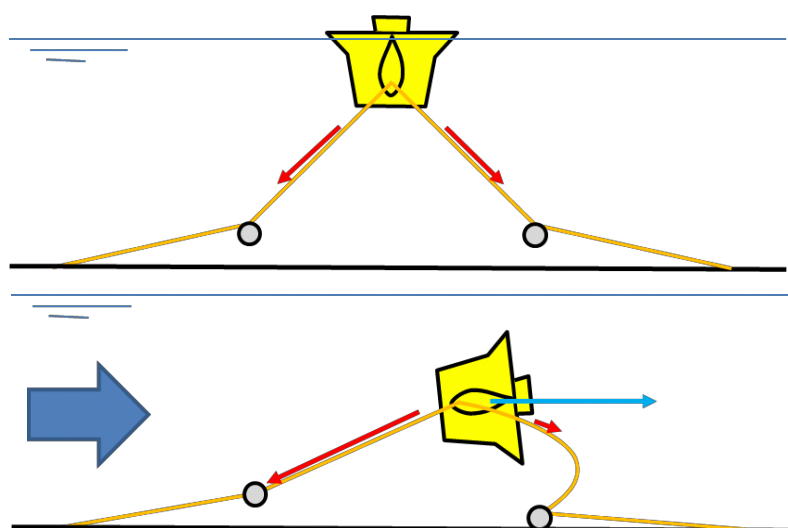

Fig. 1-7 Current stop

Fig. 1-8 Outgoing current

Fig. 1-9 Mooring system

1.4.3. Wind lens technology

This new tidal current turbine applies wind lens technology [12]. Wind lens is developed by Prof. Ohya in Kyushu University, which aims at increasing efficiency of wind power generation [13][14][15]. This technology increases the wind velocity inside the diffuser. In this section, I explain the mechanism of wind lens technology briefly.

Wind lens turbine consists of a diffuser shroud with a broad ring brim at the exit periphery and a wind turbine inside it as shown Fig. 1-10.

The diffuser shroud with a large brim is able to increase the wind speed inside the diffuser[16] from approaching wind substantially by flow mechanics reasons, e.g., the generation of low pressure region by vortex formation, flow entrainment by vortices and so on, of the inner or peripheral flows around the diffuser shroud, as shown in Fig. 1-10.
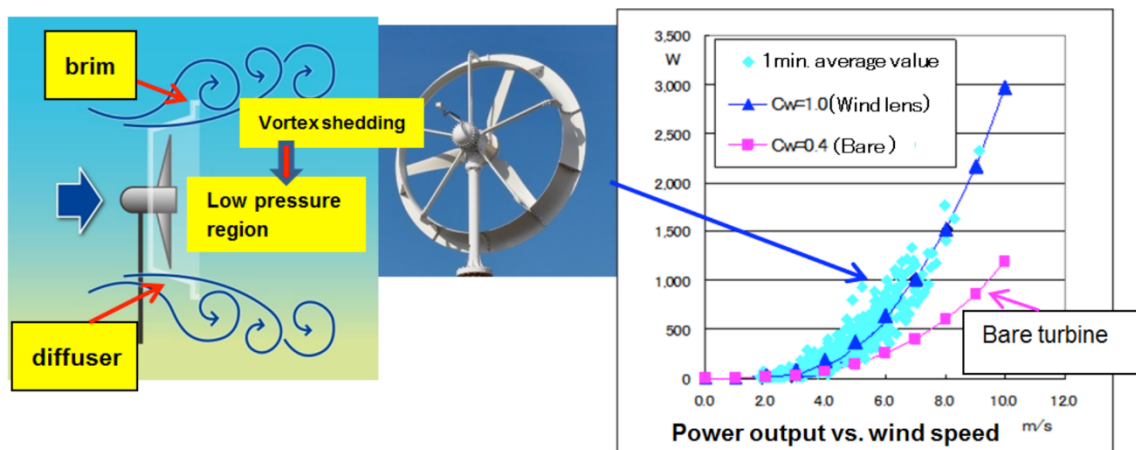

Fig. 1-10 Wind lens turbine, the mechanism, and its performance. [12]

1.5. Purpose of this study

In our laboratory, a feasibility study on this new type tidal current turbine has been carried out[17]. However, we need to carry on a further study to improve the efficiency of the tidal current turbine for practical application.

In this study, as a continuation of the previous research, I focus on optimization of the diffuser shape. Particularly I want to find the influence of the diffuser thickness on the flow velocity increase inside the diffuser and the drag force on the diffuser by using CFD simulation. OpenFOAM is used for the numerical simulation.

After that, a numerical simulation on a diffuser augmented turbine model is carried out to examine the effect of the turbine rotation.

1.6. Outline of the study

This thesis is comprised of the following parts.

The first chapter, Chapter 1, shows the energy situation in the world and special feature of the tidal current turbine. Moreover, this chapter introduces our new tidal current turbine concept.

In Chapter 2, explanation of an open source CFD code, OpenFOAM (Open Source Field And Manipulation) which is a C ++ toolbox using numerical fluid dynamics and a finite-element mesh generator.

In Chapter 3, we show about three numerical diffuser models for this calculation. Moreover, we are going to explain a setting of this calculation.

Chapter 4 is a result and discussion part. We analyze the result using average velocity ratio inside the diffuser, drag force, streamline, vorticity and pressure distribution.

In Chapter 5, we show a process and result of numerical analysis for a rotating area.

Finally, conclusions of this research are shown in Chapter 6.

Chapter 2: Methodology

In this chapter, the software are explained which were used to calculate in this study.

First of all, computer information is introduced which is used in this research.

Rhinoceros(3D CAD) is used when numerical models were designed. Also, the meshes are generated by Gmsh. The numerical calculation is performed using OpenFOAM. Therefore, we explain each software step by step.

First, we explain about Rhinoceros simply.

After that, we explain a generation method of meshes. The meshes are generated by Gmesh. We show some information about Gmesh.

In OpenFOAM section, the details of CFD simulation governing equations, turbulence model and wall boundary condition are explained.

2.1. Specification of PCs

Three PCs were used in parallel because a lot of cases needed to be calculated within the limited time. The specifications of the four PCs are shown in Table 2-1 to 2-3.

Table. 2-1 The specification of PC no. 1

Manufacturer	DELL
Model	Optiplex 9020
CPU	Intel® Core™ i7-4790 @ 3.60 GHz
RAM	8.00 GB
OS	Windows 10

Table. 2-2 The specification of PC no. 2

Manufacturer	Hewlett-Packard
Model	Z420 Workstation
CPU	Intel® Xeon® CPU E5-1620 v2 @ 3.70 GHz
RAM	8.00 GB
OS	Windows 10

Table. 2-3 The specification of PC no. 3

Manufacturer	Hewlett-Packard
Model	Z800 Workstation
CPU	Intel® Xeon® CPU X5680 @ 3.33 GHz
RAM	24 GB
OS	Windows 10

2.2. Rhinoceros

Rhinoceros (Rhino)[18] is a commercial three-dimensional CAD software (3D surface modeler) for manufacturing that is specialized for free-form NURBS modeling. Rhinoceros is generally used not only in industrial design, architecture, shipbuilding, jewelry design, car design, CAD / CAM, rapid prototyping, reverse engineering, product design but also in the multimedia design and graphic design industry. In this study, I designed some different shape diffusers. In chapter. 3, we explain the detail of numerical models.

2.3. Gmsh

Meshes can be generated using program (block mesh and snappyHexMesh) in OpenFOAM. However, the aspect ratio of some mesh becomes exceptionally high because of a shape of meshes around diffuser becomes, which may affect calculation time and calculation accuracy. In this study, meshes generated by Gmsh and SALOME. I explain about both mesh generator in this section.

Gmsh is a three-dimensional finite element mesh generator with built-in pre- and post-processing facilities developed by Christophe Geuzaine and Jean-Francois Remacle. Gmsh consists of four modules: geometry, mesh, solver, and post-processing. [19] Since it is assumed to be used as a mesh generator, Gmsh is aimed at generating mesh data and save it. The most significant point is that it is possible to adjust the division number for each side of the calculation area, thereby changing the size and density of the mesh. In this study, meshes around the diffuser are finer than other regions. In three-dimensional case, it seems that if Gmsh is used, mesh data with complicated settings can be generated relatively quickly.

Next, we explain how to define the condition of the mesh briefly.
First, the area where the fluid flows is defined.
Second, face groups are named. This step is essential because boundary conditions are decided depends on each face type when the setting of CFD is defined.

2.4. SALOME

In the simulation using the rotating mesh shown in Chapter 5, mesh generation is performed using SALOME[20]. One of the big reasons is that it is used in the rotating mesh tutorial around the turbine. Also, our laboratory has an environment where I can receive technical support about mesh generation using SALOME. That is also the reason. SALOME is a Linux-based open source structure / thermal analysis software provided by EDF (Électricité de France)[21]. Analysis solver uses Code_Aster and has highly advanced and varied functions mainly on structural mechanics and thermodynamics and has over 400 elements (1 dimensional, 2 dimensional, 3 dimensional, et cetera). Besides, there are over 2000 test cases, training texts and more than 13000 pages of documents (usage method, technique, theoretical background), official forum, etc. Compared with other open source CAE software, the support system is enriched.

2.5. OpenFOAM

This study is performed with OpenFOAM(Open Field Operation and Manipulation)[22][24]. OpenFOAM (Open Source Field Operation And Manipulation) is an open-source Computational Fluid Dynamics (CFD) toolbox published by the GNU General Public License (GPL). It is a class library for various partial differential equation solver development Oriented Programming Language C ++, and realizes high descriptiveness and extensibility with C ++ syntax. When we use the standard solver, we can do the following calculations.

· Steady / Unsteady turbulent incompressible flow analysis
· Steady / Unsteady heat convection analysis of compressible fluids
· Fluid / solid heat transfer (CHT) analysis
· Multiphase flow analysis (interface tracking method / multi-fluid model)

2.5.1. Governing equations

To simulate physical phenomena in numerical calculations, the fundamental equations which govern these physical problems need to solve under given initial condition and boundary conditions. The following governing equations are used in incompressible fluid flow analyses.

(1) Mass conservation equation

$$\frac{\partial u_i}{\partial x_i} = 0 \tag{2.1}$$

(2) Momentum conservation equation (Navier-Stokes equation, i=1-3)

$$\frac{\partial \rho u_i}{\partial t} + \frac{\partial u_j \rho u_i}{\partial x_j} = -\frac{\partial p}{\partial x_i} + \frac{\partial}{\partial x_j} \mu \left(\frac{\partial u_i}{\partial x_j} + \frac{\partial u_j}{\partial x_j} \right) - \rho g_i \beta (T - T_0) \tag{2.2}$$

(3) Turbulence model equation

The turbulence model is discussed in section 2.5.2.

2.5.2. Turbulence model

SST k-ω model is solved k-ω model in the vicinity of wall and k-ε model in the mainstream. The feature of k-ω model is that k-ω model is good at a region of the wall. It means k-ω model is fit on viscous sublayer. Moreover, the k-ε model can solve the main flow accurately. Each effective range is utilized. Also, the k-ε model is a quadratic equations model. Following turbulence energy k and turbulence dissipation rate ε are derived from Reynolds Averaged Navier-Stokes equation in k-ε model.

$$k = \frac{1}{2} \frac{\partial \overline{u_i'^2}}{\partial x_j} \tag{2.3}$$

$$\varepsilon = \gamma \left(\frac{\partial \overline{u_i}}{\partial x_j} \right)^2 \tag{2.4}$$

Equation about k in k-ε model and ε in k-ω model are shown in equation (2.5) and (2.6).

$$\frac{\partial \rho k}{\partial t} + \frac{\partial u_i}{\partial x_i} \left[\left(\mu + \frac{\mu_t}{\sigma_k} \right) \frac{\partial k}{\partial x_i} \right] + G_s - \rho \varepsilon \tag{2.5}$$

$$\frac{\partial \rho \varepsilon}{\partial t} + \frac{\partial u_i \rho \varepsilon}{\partial x_i} = \frac{\partial}{\partial x_i} \left[\left(\left(\mu + \frac{\mu_t}{\sigma_k} \right) \frac{\partial \varepsilon}{\partial x_i} \right) \right] + C_1 \frac{\varepsilon}{k} G_s - C_2 \frac{\rho \varepsilon^2}{k} \tag{2.6}$$

Equation about k in k-ω model and turbulence dissipation rate per energy ω are shown in equation (2.7) and (2.8).

$$\frac{\partial \rho k}{\partial t} + \frac{\partial u_i k}{\partial x_i} = \frac{\partial}{\partial x_i} \left[\left(\mu + \frac{\mu_t}{\sigma_{k1}} \right) \frac{\partial k}{\partial x_i} \right] + G_s - \rho C t k \omega \tag{2.7}$$

$$\frac{\partial \rho \omega}{\partial t} + \frac{\partial u_i \omega}{\partial x_i} = \frac{\partial}{\partial x_i} \left[\left(\mu + \frac{\mu_t}{\sigma_{k1}} \right) \frac{\partial \omega}{\partial x_i} \right] + \frac{\gamma_1 \rho}{\mu_t} G_s - \rho \beta_1 \omega^2 \tag{2.8}$$

Where,

$$G_s = \mu_t \left(\frac{\partial \bar{u}_\iota}{\partial x_j} + \frac{\partial \bar{u}_j}{\partial x_i} \right) \frac{\partial \bar{u}_\iota}{\partial x_j} \tag{2.9}$$

$$\mu_t = \rho C_t \frac{k}{\omega} \tag{2.10}$$

$$\gamma_1 = \frac{\beta_1}{C_t} - \frac{\kappa^2}{\sqrt{Ct\sigma_{\omega 1}}} \tag{2.11}$$

Following equation is derived by to assume $\varepsilon = k\text{-}\omega$ in k-ε model.

$$\frac{\partial \rho k}{\partial t} + \frac{\partial u_i \rho k}{\partial x_i} = \frac{\partial}{\partial x_i} \left[\left(\mu + \frac{\mu_t}{\sigma_{k2}} \right) \frac{\partial k}{\partial x_i} \right] + G_s - \rho Ctk\omega \tag{2.12}$$

$$\frac{\partial \rho \omega}{\partial t} + \frac{\partial u_i \rho \omega}{\partial x_i} = \frac{\partial}{\partial x_i} \left[\left(\mu + \frac{\mu_t}{\sigma_{\omega 2}} \right) \frac{\partial \omega}{\partial x_i} \right] + \frac{\gamma_2 \rho}{\mu_t} G_s - \rho \beta_2 \omega^2 + 2 \frac{\rho}{\sigma_{\omega 2} \omega} \frac{\partial k}{\partial x_j} \frac{\partial \omega}{\partial x_j} \tag{2.13}$$

Where,

$$\gamma_2 = \frac{\beta_2}{C_t} - \frac{\kappa^2}{\sqrt{Ct\sigma_{\omega 2}}} \tag{2.14}$$

Then, the mixing function is defined as the following equation.

$$F_1 = \tanh(\arg_1^4) \tag{2.15}$$

Where,

$$\arg_1 = \max\left(min\left(\frac{\sqrt{k}}{0.09\omega y}, 0.45 \frac{\omega}{\Omega} \right), \frac{400\gamma}{y^2 \omega} \right) \tag{2.16}$$

From equation (2.7)×F_1+equation (2.12)×(1−F_1), equation (2.17) is leaded, from equation (2.8)×F_1 + equation (2.13)×(1 − F_1), equation (2.18) is leaded, SST k-ω model is expressed following equations.

$$\frac{\partial \rho k}{\partial t} + \frac{\partial u_i \rho k}{\partial x_i} = \frac{\partial}{\partial x_i} \left[\left(\mu + \frac{\mu_t}{\sigma_k} \right) \frac{\partial k}{\partial x_i} \right] + G_s - \rho Ctk\omega \tag{2.17}$$

$$\frac{\partial \rho \omega}{\partial t} + \frac{\partial u_i \rho \omega}{\partial x_i} = \frac{\partial}{\partial x_i} \left[\left(\mu + \frac{\mu_t}{\sigma_\omega} \right) \frac{\partial \omega}{\partial x_i} \right] + \frac{\gamma_2 \rho}{\mu_t} G_s - \rho \beta_2 \omega^2 + 2(1 - F_1) \frac{\rho}{\sigma_{\omega 2} \omega} \frac{\partial k}{\partial x_j} \frac{\partial \omega}{\partial x_j} \tag{2.18}$$

In view of superiorities of the SST k-ω model, it should be the model of choice for hydrodynamic applications. In this study, the SST k-ω model is chosen as the turbulence model.

Chapter 3: Numerical analysis

This chapter shows models and initial settings used in this simulation. How it was set in OpenFOAM is also shown. First, diffuser models which are used in this calculation are explained and information about models are shown. Second, a setting of the calculation is shown step by step. Third, the convergence check of the meshes is shown.

3.1. Diffuser models

In this study, 3 different shape models are designed. The first model is the original model as shown Fig. 3-1 to 3-3. The original model was used in an experiment last year. In the experiment of last year, basic experiments on the feasibility of this new tidal power turbine were carried on. Good results have been obtained regarding feasibility study[17]. This numerical simulation is performed using a model which is the same size as the experimental model. The scale of the experimental model is 1/6. Other features of the original model are as shown in Table. 3-1. In the CFD simulation, a turbine is not considered for simplicity.

Table. 3-1 Information of the original model

Inside diameter	0.4 [m]
Outside diameter	0.14 [m]
Length	0.22 [m]
Volume	1.178 [m^3]
Thickness of the diffuser	0.05 [m]
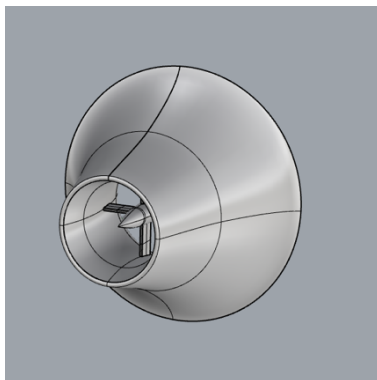
Fig. 3-1 Perspective view of the original model
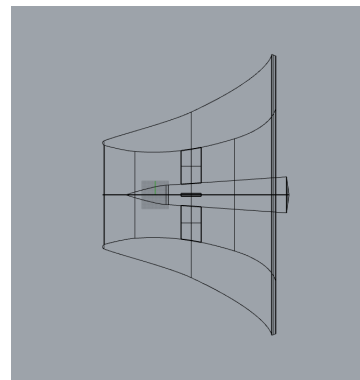
Fig. 3-2 Side view of the original model
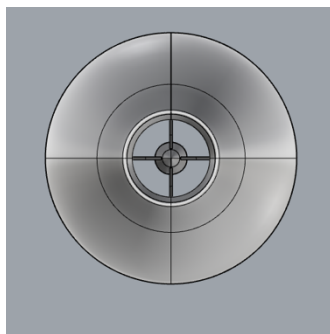
Fig. 3-3 Front view of the original model

However, the original model is designed to aim to gain enough buoyancy force to make steady the device. 2 different diffuser models are designed to find the relation between the thickness of the diffuser and current velocity inside the diffuser. One is the slim model. A thickness of the slim model is thin. Inside diameter, Outside diameter and length are the same sizes as the original model. A volume of the slim model is approximately 22.5 % lower than the original model. Features of the slim model are as follows. The other is the fat model. A thickness of the fat model is thick. Outside diameter and length are also the same sizes as the original model. A volume of the fat model is approximately 57 % larger than the original model.

Table. 3-2 Information of the slim model

Inside diameter	0.4 [m]
Outside diameter	0.14 [m]
Length	0.22 [m]
Volume	0.789 [m^3]
Thickness of the diffuser	0.03 [m]
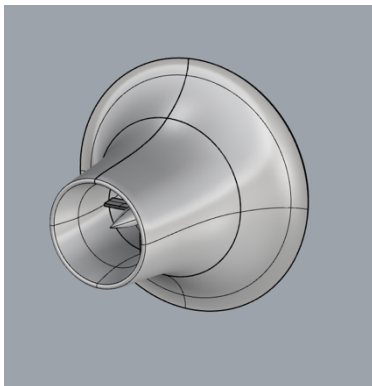
Fig. 3-4 Perspective view of the slim model
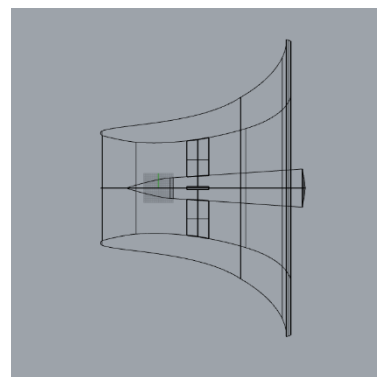
Fig. 3-5 Side view of the slim model
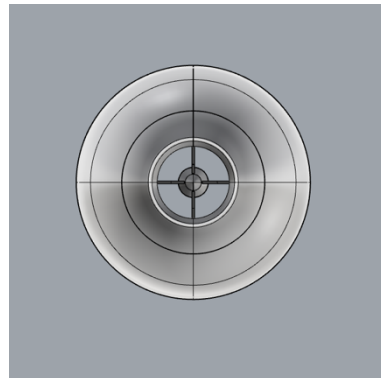
Fig. 3-6 Front view of the slim model

Table. 3-3 Information of the fat model

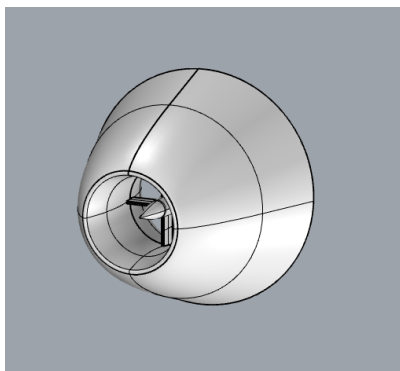|	
Inside diameter	0.4 [m]
Outside diameter	0.14 [m]
Length	0.22 [m]
Volume	1.85[m^3]
Thickness of the diffuser	0.09 [m]

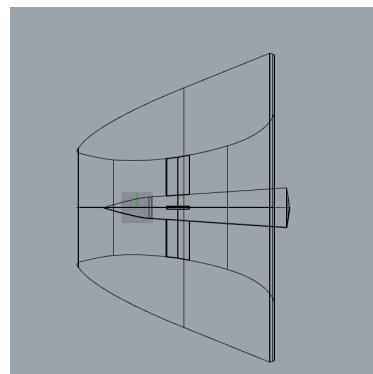Fig. 3-7 Perspective view of the fat model

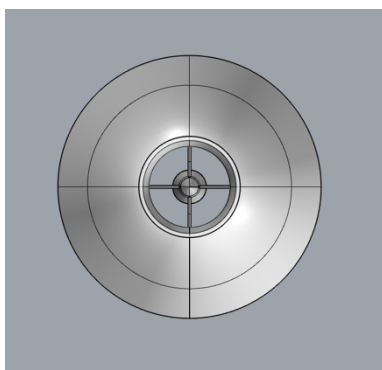Fig. 3-8 Side view of the fat model

Fig. 3-9 Front view of the fat model

3.2. Setting of the calculation

In this section, we explain about boundary box, boundary condition, and calculation setting step by step.

3.2.1. The computational domain

The computational domain is constructed for this calculation as shown in Fig. 3-10.
The installation position of the diffuser was decided to take a large area behind the diffuser in order to observe the wake flow well.
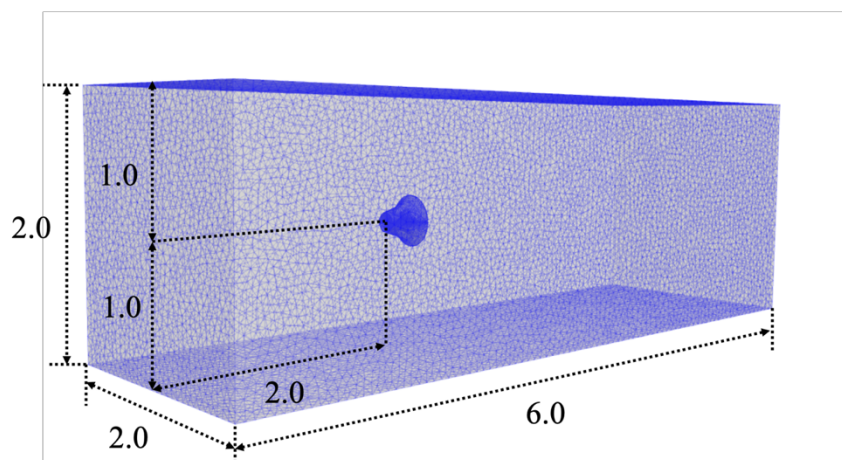
Fig. 3-10 Computational domain

3.2.2. Boundary conditions

In this calculation, a slip is specified at the side walls, bottom, and upper side. The slip condition makes the flow on the wall. The constant static pressure of 0 [Pa] is set across the outlet. Density of the fluid is 999.741 [kg / m^3] and coefficient of kinematic viscosity is 1.10×10^{-6} [m^2 / s].

The flow velocity at the inlet are defined between 9.0 [m / s] and 15 [m / s] at 0.6 [m / s] intervals based on similarity law of Reynolds. We assume that current velocity of the area scheduled for installation is between 1.5 [m / s] and 2.5 [m / s]. The turbulence intensity is 10 %, and turbulent kinetic energy k [m^2 / s^2] is calculated by following Eq. 3-1. Here U [m / s] is the flow velocity, *and I* is the turbulence intensity = 10. The kinetic energy ω [s^{-1}] is calculated by Eq. 3-2. In the Eq. 3-2, the viscosity ratio μ / μ_t is defined 10. The actual values used for this calculation are shown in table. 3-4.

$$k = \frac{3}{2}(UI)^2 \qquad (3\text{-}1)$$

$$\omega = \frac{\rho k}{\mu} \frac{\mu}{\mu_t} \qquad (3\text{-}2)$$

Table. 3-4 Initial value and physical property value for the numerical calculation

The velocity in the ocean [m / s]	The flow velocity for this calculation [m / s]	turbulent k [m^2 / s^2]	turbulent ω [s^{-1}]	Re
1.5	9.0	0.3037	2,745,013.374	1.616×10^6
1.6	9.6	0.3456	3,123,215.217	1.717×10^6
1.7	10.2	0.3901	3,525,817.178	1.818×10^6
1.8	10.8	0.4374	3,952,819.259	1.919×10^6
1.9	11.4	0.4873	4,404,221.458	2.020×10^6
2.0	12.0	0.5400	4,880,023.776	2.121×10^6
2.1	12.6	0.5953	5,380,226.213	2.222×10^6
2.2	13.2	0.6534	5,904,828.769	2.323×10^6
2.3	13.8	0.7141	6,453,831.444	2.424×10^6
2.4	14.4	0.7776	7,027,234.237	2.525×10^6
2.5	15.0	0.8437	7,625,037.150	2.60×10^6

3.2.3. Time step

When the time step is decided, Courant number is a significant factor. In flow calculation, Courant number shows how many elements the flow goes in one cycle. As the number of Courant number is large, accuracy of the calculation lacks markedly Here flow velocity is u, a time interval is Δt, and element width is Δl, Courant number C can be obtained by the following formula Eq. 3-3.

$$C = \frac{u\Delta t}{\Delta l} \qquad (3\text{-}3)$$

In this calculation, minimum mesh size is 0.0427. Therefore, the time step is 0.00005 so that the Courant number should not be larger than 1.

3.2.4. Mesh generation

The mesh size is quite important for getting an accuracy of the numerical simulation. Moreover, an effective mesh can save the calculation time. For these purposes, the convergence check of the mesh is performed. In this convergence check, three different meshes are generated. Drag coefficient is calculated and used to evaluate mesh convergence. The result of the convergence check is shown in Fig. 3-11.

The drag coefficients become constant according to increased mesh size. A mesh which has the largest number of cells is used in this calculation. The number of the mesh is 1,036,937, and the minimum cell size is 0.0427. In this convergence check, the original model is used. In other cases (slim model, thick model), the meshes have the approximately same number of cells shown as Table. 3-2. Therefore, the accuracy of this simulation is enough. Moreover, the mesh distribution surrounding diffuser is shown in Fig.3-12.
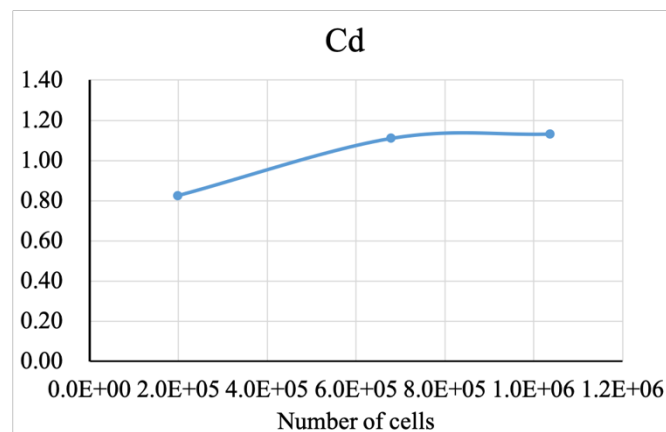

Fig. 3-11 Drag coefficient for the convergence check

Table. 3-2 The number of cells

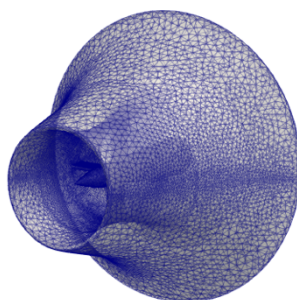|	Original model	Slim model	Thick model
Number of cells	1,036,937	1,124,021	1,049,686

Fig. 3-12 Mesh distribution on the diffuser

3.2.5. Solver

In OpenFOAM we can set solver with file fvSlutions for pressure and flow velocity et cetera respectively. We used GAMG (geometric-algebraic multi-grid) and smoothSolver (Gauss-Seidel method) which can be solved at high speed as it is necessary to perform multiple numerical calculations. It is also possible to specify the calculation termination condition due to the residual. In this calculation, it is set as shown below. When the residual is less than 1.0×10^5 with respect to pressure, the calculation is terminated.

```
{
    "pcorr.*"
    {
        solver          GAMG;
        tolerance       1e-2;
        relTol          0;
        smoother        DICGaussSeidel;
        cacheAgglomeration no;
        maxIter         50;
    }

    p
    {
        $pcorr;
        tolerance       1e-5;
        relTol          0.01;
    }
```

3.2.6. Parallel calculation

In OpenFOAM, it is possible to set parallel calculation with a file decomposePar.
You can set how many CPUs to use, and how many areas are divided into the x, y, z-direction. How many CPUs are used to calculate depends on the specification of the PC to be used, but we show the setting when using six CPUs below. In the current calculation, since it is a calculation region that is long in the x-axis direction, we set the x-axis direction to the largest number of divisions.

```
numberOfSubdomains 6;

method          hierarchical;

hierarchicalCoeffs
{
    n               (3 2 1);
    delta           0.001;
    order           xyz;
}
```

3.2.7. Setting of calculating coefficient

In this calculation, drag coefficients are calculated and compared. The various conditions necessary for this calculation can be set with a file named forcecoeff. For example, the values used when the flow velocity is 9.0 [m / s] are shown in Table 3-3. Besides, the part where the actual file is set up is shown below. RhoInf means a density of the fluid, 999.741 [kg / m^3] which is the density of water at 10 °C because we will compare with the experimental result next year is used.

Table. 3-3 Values for calculating drag coefficient

Density of the fluid	999.741 [kg/m^3]
Direction of lift	Z direction
Direction of drag	X direction
The center point	(0, 0, 0)
Axis of pitch	Y axis
Magnitude of velocity	9.0 [m/s]
Characteristic length	0.22 [m]
Projected area	0.1257 [m^2]

```
  writeControl    timeStep;
    timeInterval    0.1;

    log             yes;

    patches         (motorbikegroup);
    pName           p;
    UName           U;
    rho             rhoInf;      // Indicates incompressible
    rhoInf          999.741;         // Redundant for incompressible
    liftDir         (0 0 1);
```

```
dragDir     (1 0 0);
CofR        (0 0 0);  // Axle midpoint on ground
pitchAxis   (0 1 0);
magUInf     9;
lRef        0.22;          // Wheelbase length
Aref        0.125663706;       // Estimated
/*
```

Chapter 4: Results and discussion

As an example of the result, the flow velocity is 9.0 [m / s] and Re = 1.51×10^6. Results of velocity and the pressure are shown in Fig. 4-1 and 4-2, respectively. The fluid flows from the left side to the right side in the figure. The flow velocity inside the diffuser is increased compared with the flow velocity in the surrounding area. This is considered to be the effect of wind lens technology. Also, it can be seen that the flow is separating from around the brim. It is thought that this separation is responsible for creating a vortex behind the diffuser. Discussion about vortices is done in 4.3 using vorticity calculations. Subsequently, from the pressure distribution, a negative pressure region is also formed behind and inside of the diffuser, and the principle of the wind lens is confirmed. The relation between the thickness and the performance of the diffuser will be discussed below using these results.

Also, Fig. 4-3 shows the calculation results of streamline. Although this calculation is a three-dimensional calculation, it is useful to conduct a study by comparing the results of cross-sections as shown in Figs. 4-1 and 4-2.
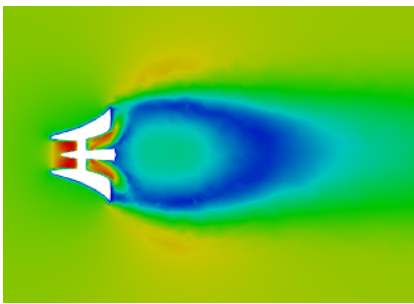
Fig. 4-1 The result of velocity at x-y plane
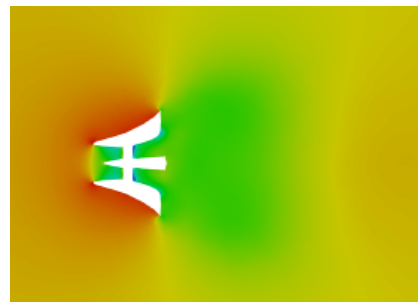
Fig. 4-2 The result of pressure
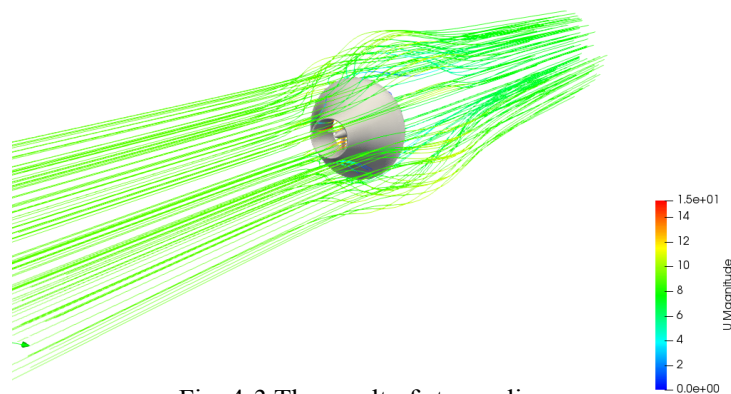
Fig. 4-3 The result of stream line

4.1. Average velocity ratio inside the diffuser

Calculations were performed for 11 patterns inlet flow velocity are between 9.0 [m / s] and 15 [m / s] using each model. Here, in addition to the flow velocity, 9.0 [m / s] is shown in Fig. 4-4, representative flow velocity distributions of 15 [m / s] are shown in Fig. 4-5. In all of the results the flow velocity inside the diffuser is increased compared to the surrounding flow velocity.
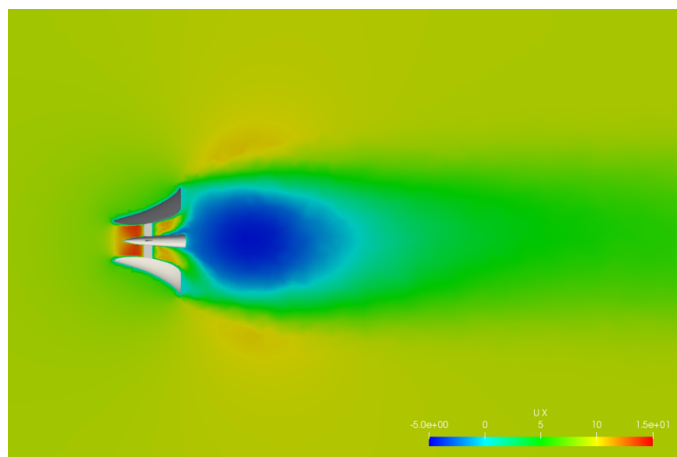

Fig. 4-4 (a) Velocity distribution 9.0 [m / s] (the original model)
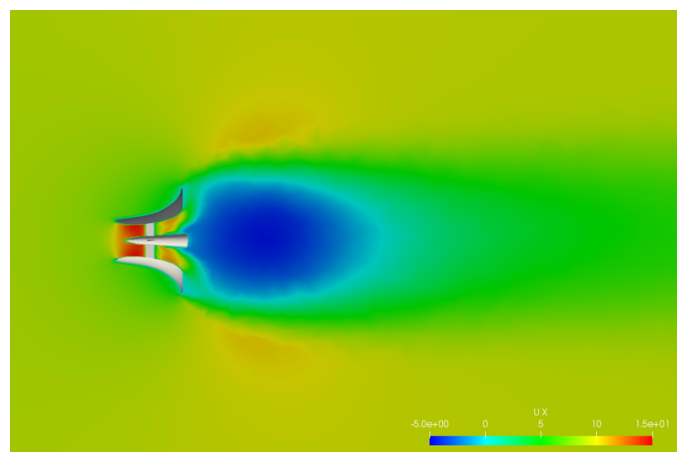
Fig. 4-4 (b) Velocity distribution 9.0 [m / s] (the slim model)
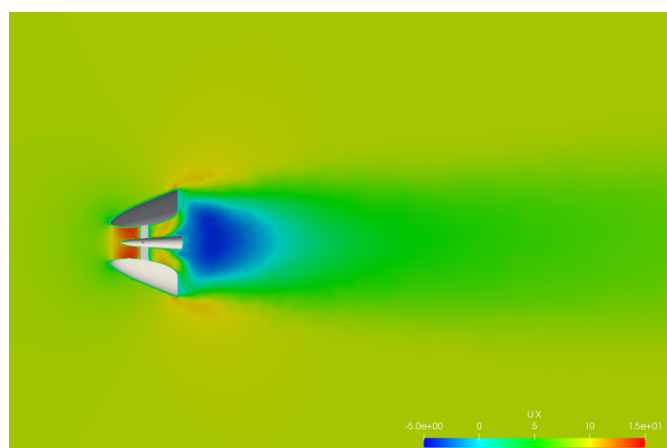
Fig. 4-4 (c) Velocity distribution 9.0 [m / s] (the fat model)
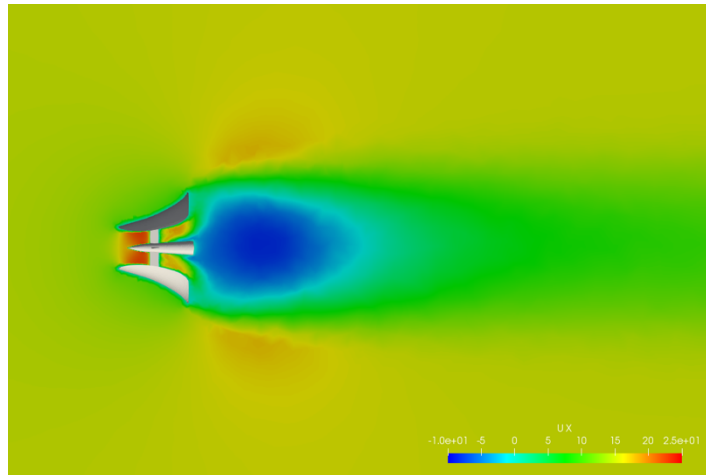
Fig. 4-5 (a) Velocity distribution 15 [m / s] (the original model)
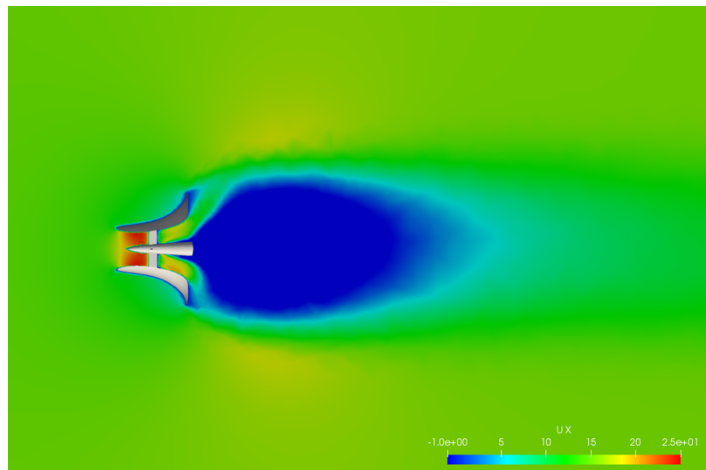
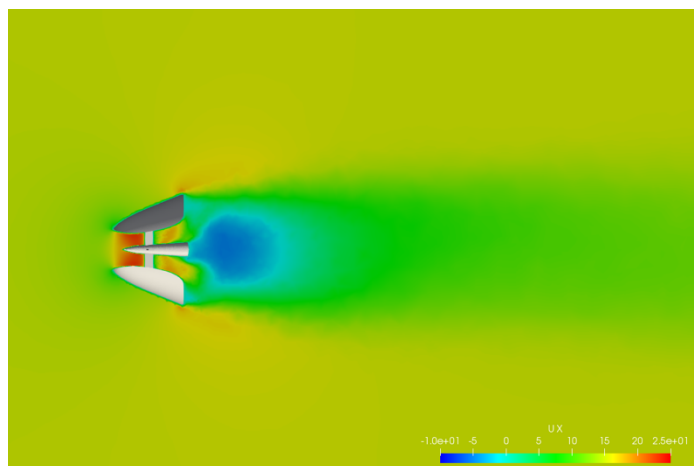Fig. 4-5 (b) Velocity distribution 15 [m / s] (the slim model)

Fig. 4-5 (c) Velocity distribution 15 [m / s] (the fat model)

Compared among the three diffuser shapes, the flow velocity behind the diffuser is negative in all cases. Moreover, when using the slim model, the low-pressure region is the largest. Regarding the flow in this area, we will investigate again using vorticity and streamline. Also, in the case of the slim model, the flow separated by the brim is pushed further to the outside of the diffuser. On the other hand, in the case of the fat model, the region where the flow velocity is negative is considerably small.

One of the essential values to evaluate the performance of all the diffusers is average velocity ratio inside the diffuser which is calculated using Eq. (4-1). Here U_∞ is the inlet velocity, U is the average velocity inside the diffuser. Here, the derivation of the average flow velocity inside the diffuser will be described. A cross-section at x = 0 is used to calculate average velocity because a turbine is attached at this point. It is necessary to use this cross section to estimate flow velocity and power generation. First, the area of one cell and the sum of the total area are calculated. Moreover, flowrate is calculated by multiplying the area of each cell and velocity in the direction of the x-axis of each cell. Finally, average velocity inside the diffuser is calculated by dividing the sum of flow rate by the total area inside the diffuser.

.

$$A = \frac{U}{U_\infty} \qquad (4\text{-}1)$$

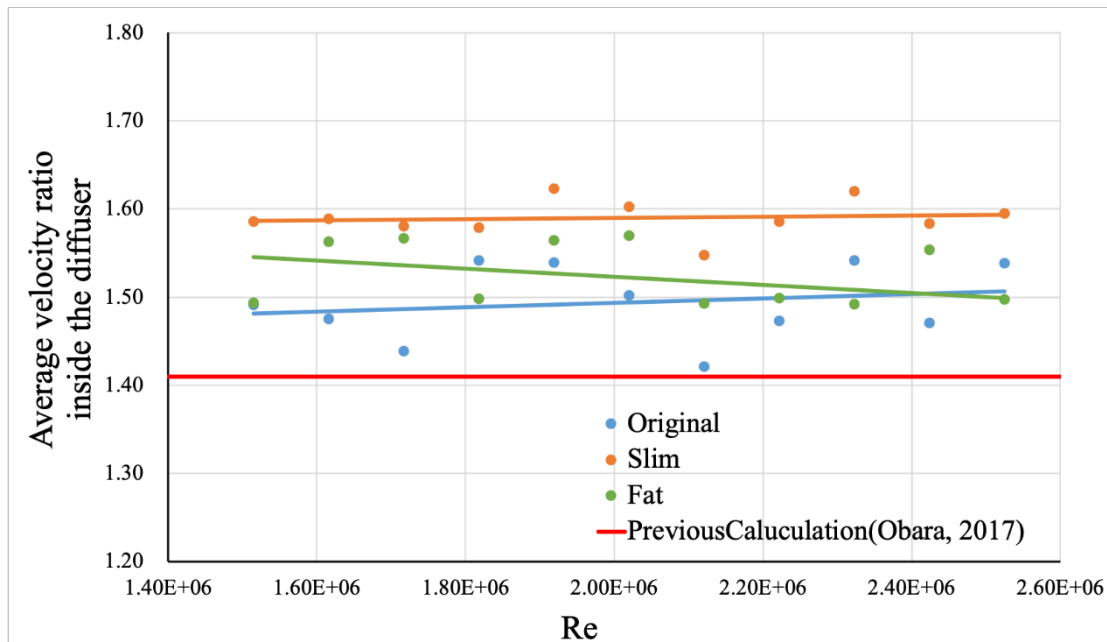The result of average velocity ratio inside the diffuser is shown in Fig. 4-6.

Fig. 4-6 Average velocity ratio inside the diffuser

The blue line shows a result of the original model, the orange line shows a result of the slim model, and the result in the initial examination conducted last year is shown by red lines. Also, an approximate expression is shown by the least square method. The slim model showed higher values at any flow velocity. The difference was about 6.5 % on average compared with the original model. It was confirmed that the energy is proportional to the cube of the flow velocity, so it is improved by about 20% in energy.

Ohya and Karasudani[13] have found that the flow velocity inside the diffuser is increased up to 1.8 times faster than inflow velocity in the diffuser only case without hub and nacelle. This result shows a smaller value compared to the past study. It is thought that the hub and the nacelle inside the diffuser significantly influence. The hub can block the flow partly, and the fluid flowing inside the diffuser decreases because the nacelle is attached.

Regarding the fat model, the rate of increase is smaller as the flow velocity increases. Since there are no big differences among each velocity case in the flow velocity distribution, it is necessary to consider this cause. Moreover, in high Reynolds' number, the ratio of the original model is higher than the fat model. There are some variations in calculation results throughout. It is considered that

the fineness of the mesh is insufficient and the calculation time is short. However, since the time is limited, it is a future task to consider calculation time and mesh distribution.

Moreover, there is a difference compared with the previous study result. What is considered as the primary cause is the quality of the mesh. Regarding the mesh number, it is about 1.5 times larger than the initial examination. In the initial examination, we used automatic generator using one of the functions of OpenFOAM, but in this research, we generate a mesh using Gmsh which can change the number of divisions of each line concerning the calculation area and target object. It can be inferred that the calculation precision is improved by making the meshes around the object particularly fine. However, in order to discuss the accuracy of this calculation, it is necessary to compare it with the data obtained by an experiment. This is an issue in the future.

4.2. Drag coefficient

In this section, we compare among three models using the drag coefficient. First of all, the drag coefficient is a dimensionless value obtained by using dynamic pressure, projected area, and flow velocity. Since cables moor this new tidal current turbine, the value of drag is also critical. Fig. 4-7 shows the results for each model.

Ohya et al.[24], has found that the drag coefficient of a wind turbine applied wind lens technology is between 0.4 and 0.6. This is a rather small value compared with the original model and the slim model. The reason for this is considered to be the shape of the diffuser. In the past research, the length in the horizontal direction is short, and thickness is thin compared to this new tidal turbine. It is thought that this difference in shape is the cause of the large drag coefficient.

The slim model showed the largest value. As compared with the original model, it becomes about 22% bigger, and drag force becomes big, so we need to consider including the mooring system. Besides, the fat model was minimal compared to the other two models. From the viewpoint of the mooring system, there is a possibility that the burden on the mooring system can be reduced. From this result, it was found that the shape of the diffuser significantly affected drag force. When using the principle of the wind lens, a diffuser and brim generate a vortex behind the diffuser to increase the flow velocity inside. Therefore, as the acceleration effect increases, the drag will also increase. However, in the fat model, drag force is considerably small although the rate of average velocity ratio inside the diffuser is not significantly changed. It is thought that this mechanism is not the principle of wind lens technology. We want to clarify this mechanism from streamlines, vorticity and pressure distribution.
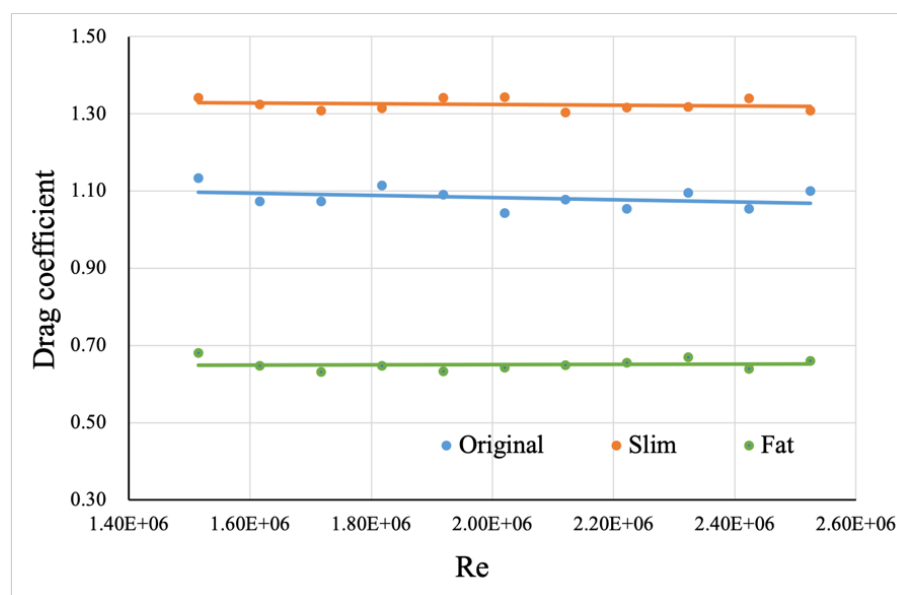

Fig. 4-7 Drag coefficient

4.3. Streamline

In this section, we investigate the cause of the difference in the flow velocity inside the diffuser and drag coefficient among three models using streamline. A streamline is a curve that makes a velocity vector of a flow field a tangent line at a certain moment. We compared the results by visualizing this streamline using paraview. First, the results of each model at a flow velocity of 9.0 [m / s], and 15[m / s] are shown in Fig. 4-8 and 4-9. These are expanded to compare the flow fields near the diffuser.
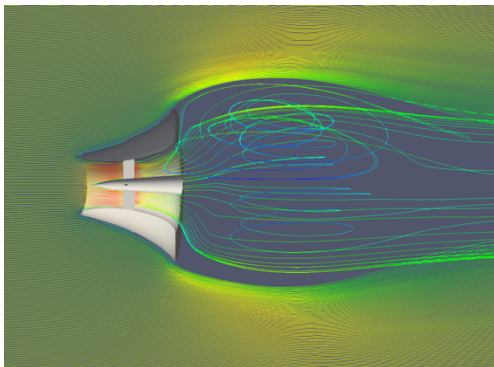
Fig. 4-8 (a) Stream line of the original model at 9.0 [m / s]
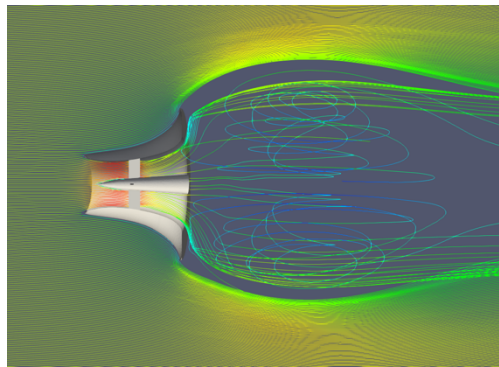
Fig. 4-8 (b) Stream line of the slim model at 9.0 [m / s]
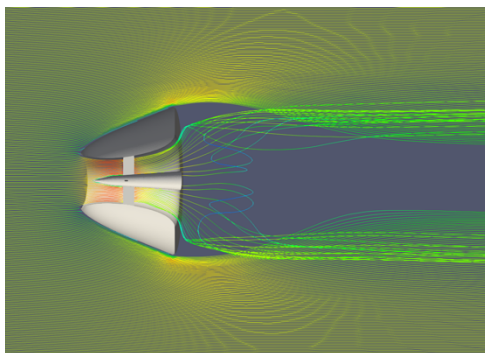
Fig. 4-8 (c) Stream line of the fat model at 9.0 [m / s]
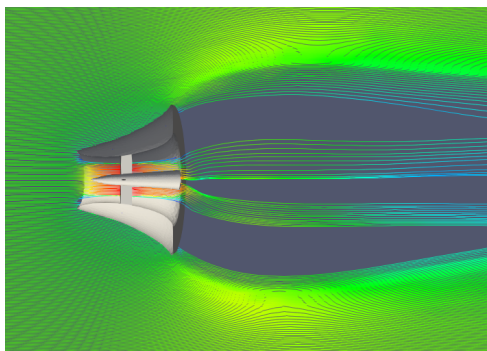
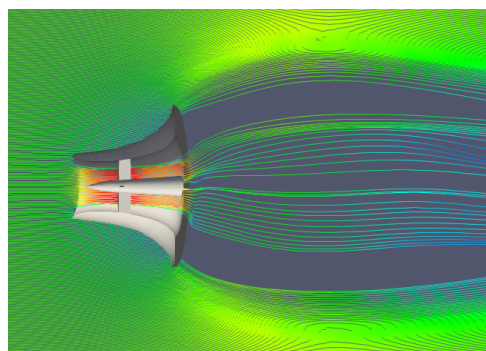Fig. 4-9 (a) Stream line of the original model at 15 [m / s]

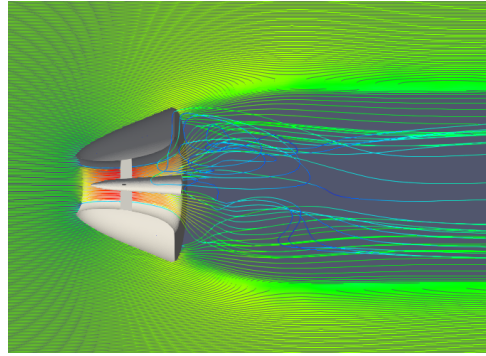Fig. 4-9 (b) Stream line of the slim model at 15 [m / s]

Fig. 4-9 (c) Stream line of the fat model at 15 [m / s]

In the case of the original model and the slim model, a vortex is formed behind the diffuser. Comparing these two models, the slim model makes larger and a distinct forms vortex. Also, paying attention to the separation point, it can be seen that in the slim model case, the flow is separates to the outer side. Shape of the brim is a critical factor in the formation of the vortex behind the diffuser. This flow influences the vortex formation. However, from this result, it was found that the flow velocity inside the diffuser of the fat model vortex is also increased as much as the original model from this result. It is clear that the original model and the slim model are increasing the internal flow velocity by the mechanism of the wind lens technology, but further study is needed on the fat model to clear the mechanism.

As the flow velocity increases, clear vortices cannot be confirmed behind the diffuser. However, flow separation can be clearly confirmed at all cases.

4.4. Vorticity

In this section, we will examine the results of each model using vorticity. Vorticity is a value representing the rotation of a flow. Vorticity is represented by a vector and is a rotation of vector field. The vorticity vector $\mathbf{\Omega}$ is expressed by the following Eq. (4-2) using the flow velocity vector $\mathbf{v} = (v_x, v_y, v_z)$

$$\mathbf{\Omega} = \text{rot } \mathbf{v} = \mathbf{\nabla} \times \mathbf{v} = \left(\frac{\partial v_z}{\partial y} - \frac{\partial v_y}{\partial z}, \frac{\partial v_x}{\partial z} - \frac{\partial v_z}{\partial x}, \frac{\partial v_y}{\partial x} - \frac{\partial x}{\partial y}\right) \qquad (4\text{-}2)$$

In developing the new tidal current power turbine which is applied the wind lens technology, the vortex behind the diffuser is also a very important factor. Therefore, comparing the vorticity behind of the diffuser is necessary to clarify the cause of the difference in the increase of the flow velocity inside the diffuser. Also, in section 4.2, we will consider the flow field of the fat model case using the vorticity results for the vortex formation behind the fat model which could not be confirmed by streamlines. Fig. 4-10 and Fig. 4-11 show the results of each model at a flow velocity of 9.0 [m / s], and 15 [m / s]. This result shows the vorticity around the z-axis in the x - y plane and the display range is between -200 and 200.
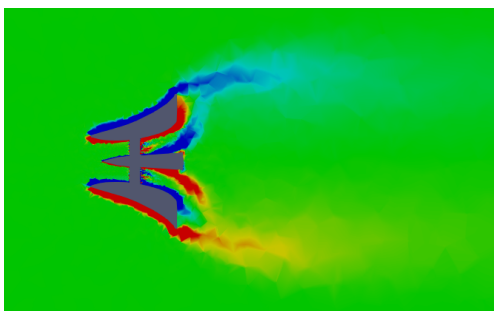
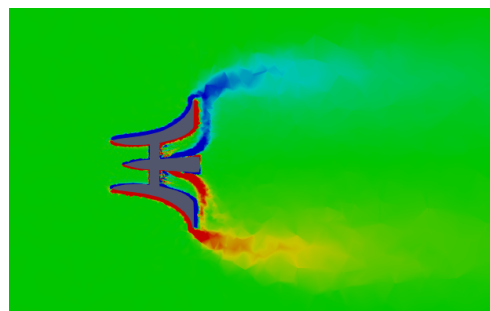Fig. 4-10 (a) Vorticity of the original
model at 9.0 [m / s]

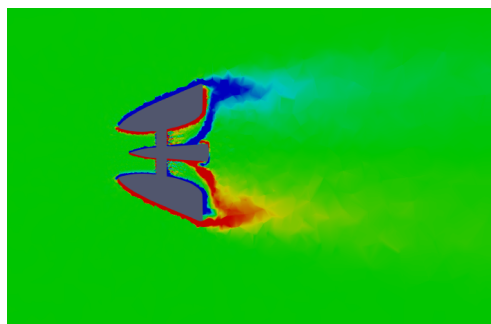Fig. 4-10 (b) Vorticity of the slim
model at 9.0 [m / s]

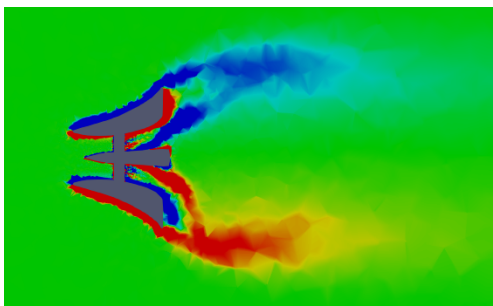Fig. 4-10 (c) Vorticity of the fat model at 9.0 [m / s]

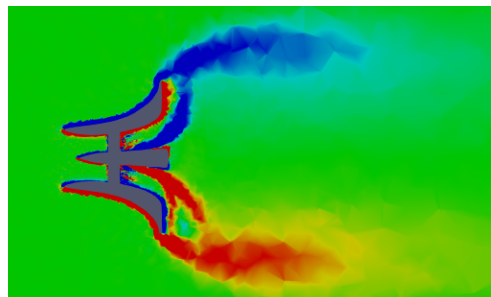Fig. 4-11 (a) Vorticity of the original
model at 15 [m / s]

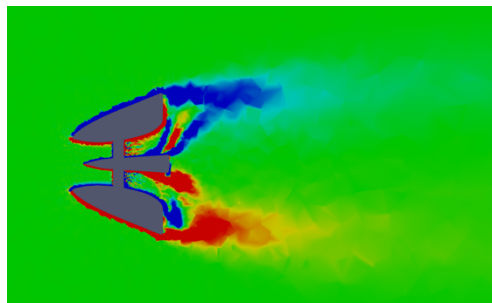Fig. 4-11 (b) Vorticity of the slim
model at 15 [m / s]

Fig. 4-11 (c) Vorticity of the fat model at 15 [m / s]

In all model cases, the vortex because of the flow separation made by the brim can be confirmed. Comparing the slim model with the original model, stronger vorticity can be confirmed at the position close to the exit behind the slim model than the original model. Although the original model can partially confirm strong vorticity, it is far from the exit of the diffuser. In the wind lens technology, the vortex creates a low-pressure region, and the velocity inside the diffuser is accelerated in a form that the fluid flows into the low-pressure region. In this study, as well as the strength of vorticity, the position where the vortex is formed is also an essential factor. That is because the pressure gradient changes the force with which the flow is drawn. A strong vortex behind the diffuser naturally draws the flow strongly, also by forming the low-pressure region at a position closer to the outlet of the diffuser, the pressure gradient also becomes larger, and the acceleration effect becomes more substantial. The element of the center of the vortex is considered to be one of the good causes of the performance of the slim model.

Moreover, the flow field including the rotation which could not be confirmed by the streamline is formed in the fat model. Although it is not a clear vortex, the flow separates from the brim, the vorticity behind the diffuser can be as large as the original model. The vorticity center is closer to the exit than the original model. As the flow velocity increases, the region with large vorticity also becomes large. It is also found that the point with the highest vorticity (the center of vorticity) moves backward.

4.5. Pressure distribution

Finally, we consider the cause of the difference in average velocity ratio inside the diffuser in each model using pressure distribution. As described above, the size and strength of the low-pressure area behind the diffuser, and its center of the low-pressure region is also a significant factor in increasing the flow velocity inside. Therefore, we analyze the results focusing on the two points. Fig. 4-12 and Fig. 4-13 show the results of each model at a flow velocity is 9.0 [m / s], and 15 [m / s].
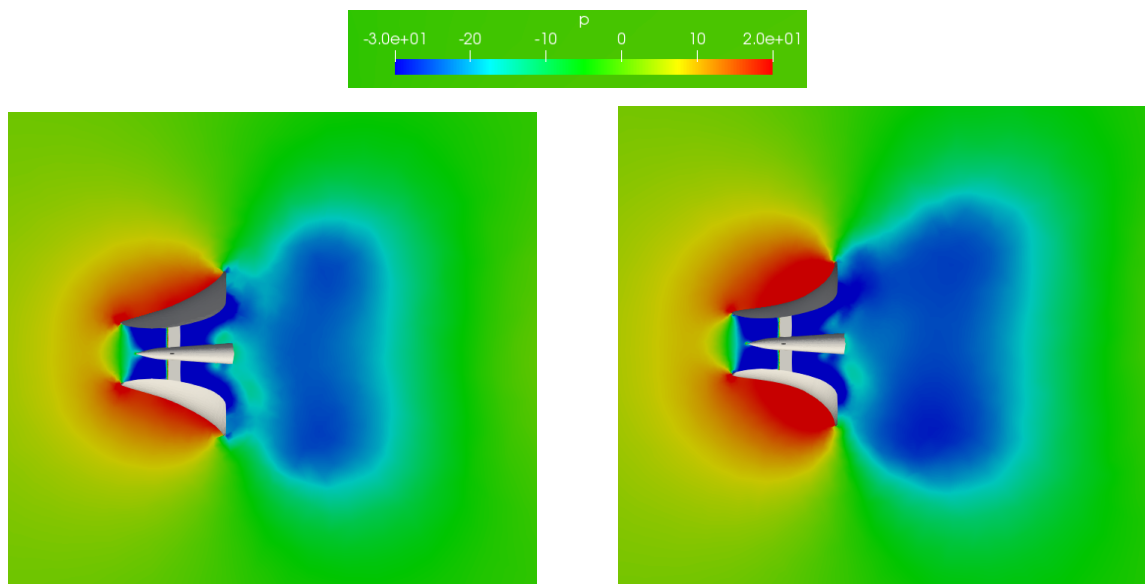

Fig. 4-12 (a) Pressure distribution of the original model at 9.0 [m / s]

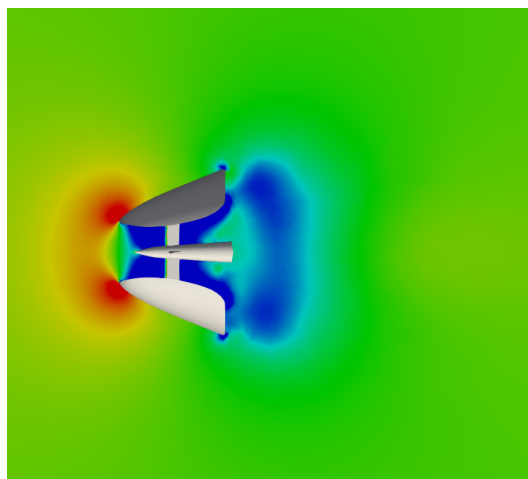Fig. 4-12 (b) Pressure distribution of the slim model at 9.0 [m / s]

Fig. 4-12 (c) Pressure distribution of the fat model at 9.0 [m / s]
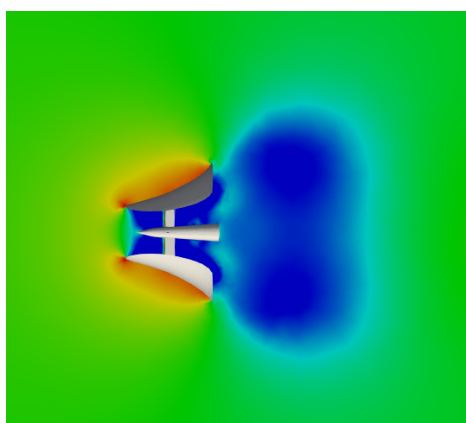

Fig. 4-13 (a) Pressure distribution of the original model at 15 [m / s]
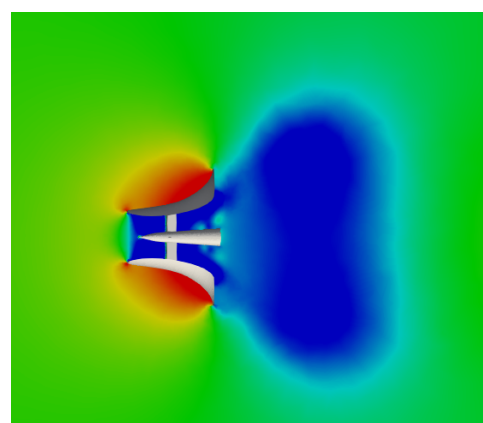

Fig. 4-13 (b) Pressure distribution of the slim model at 15 [m / s]
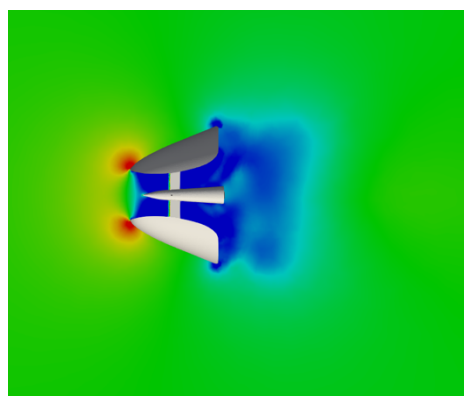

Fig. 4-13 (c) Pressure distribution of the fat model at 15 [m / s]

In all model cases, it can be confirmed that the negative pressure region is formed by the influence of the vortex formed behind the diffuser. First, the magnitude of the pressure and the size of the negative pressure region are compared. It can be seen that the lowest pressure is made in the case of the slim model. There is no big difference in the original model and the fat model about the magnitude of the negative pressure. Subsequently, in the size of the negative pressure region, the largest negative pressure area can be confirmed in the case of the slim model. In the case of the fat model, the size of the negative pressure region is the smallest. Next, we will examine the position of the center of the negative pressure region (the point with the lowest pressure). The distance from the outlet of the diffuser is essential for increasing the current velocity inside the diffuser. The closer the distance is, the larger the pressure gradient becomes and the acceleration effect increases. When comparing the original model and the slim model, there is no big difference in the center position of the negative pressure. Comparing the case of the fat model with the other two cases, it can be seen that in the case of the fat model, the center position of the negative pressure is close to the outlet of the diffuser. As a result, it is considered that the fat model with a small negative pressure region also does not result in a great difference between the acceleration effect and the original model.

The pressure at the front of the slim model is larger than that of the original model. This difference gets more prominent as the flow speed increases. Naturally, the drag force increases accordingly. Therefore, it is necessary to carefully consider current velocity zone to install in experiments in the actual sea area.

Chapter 5: Numerical analysis for rotating area

In the past section, numerical calculations have been carried out for a stable region including the diffuser and the hub. Rotating parts (the turbine) is not considered. However, in order to consider the power output performance, numerical calculation also need to be performed for the rotating region such as the turbine. Therefore, it is possible to estimate the amount of power generation. In this study, a mesh including both the rotation area (the turbine) and the stationary area (the diffuser) was created, and the numerical calculation was performed as a second step to improve.

5.1. Turbine model for numerical analysis

In this numerical calculation, a turbine model for numerical calculation simplified by referring to the turbine model used in the experiment of last year was designed. The airfoil used the same NACA 4415[17][25][26] as last year. Also, by making constant twist angle wings, curves are reduced, and the shape of the turbine is simplified to make it easy. The tip speed ratio is 4.0, the angle of attack is 10.72 °, and turbine diameter is 0.1 [m]. Fig. 5-1 shows the turbine model for numerical analysis.

5.2. Diffuser model for numerical analysis

For the convenience of time, we cannot perform numerical calculations on all diffuser models, so we use a slim model with the highest rate of Average velocity inside the diffuser. Also, we decided to not to consider for the hub connecting the diffuser and the turbine for simplicity. The diffuser and turbine models are shown in Fig. 5-1 and 5-2.
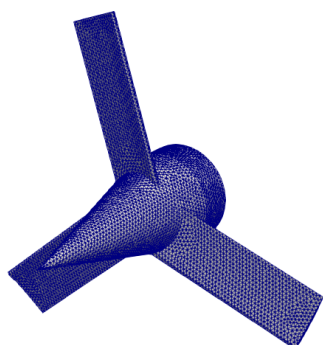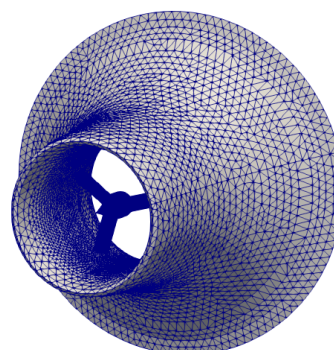
Fig. 5-1 Turbine model for numerical analysis   Fig. 5-2 Turbine and the diffuser model

5.3. Mesh generation

In this numerical calculation, a mesh was generated by SALOME. To generate a mesh which considers the rotating region we use a periodic boundary called cyclic AMI in OpenFOAM. Therefore, it is necessary to generate a mesh of a rotating region including a turbine and a stable region including a diffuser. A cylindrical area was generated in the diffuser, and a mesh of the turbine model was created in it. A mesh used for this calculation is completed by merging the rotation region as a stable region and two meshes. The boundary condition between the two regions is a periodic boundary. The calculation area was cylindrical. Fig. 5-3 shows the computational domain. Besides, the mesh number and the minimum mesh size are shown in Table 5-1.
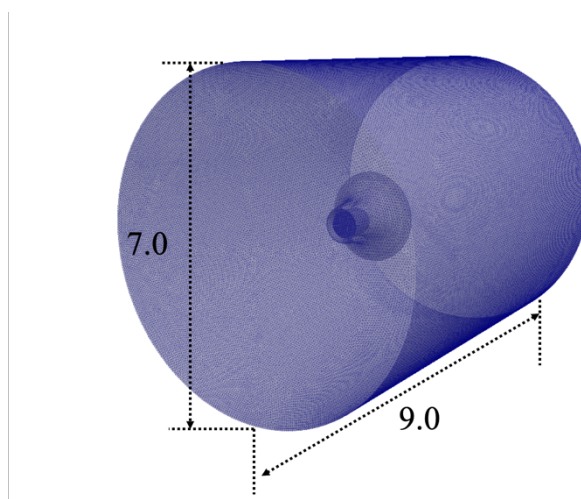

Fig. 5-3 The computational domain for rotating case

Table. 5-3 Information of the mesh

The number of mesh	2,482,889
Minimum mesh size [m]	0.004193

5.4. Setting of the calculation

In this calculation, a three-dimensional unsteady calculation was performed using solver called pimpleDyMFoam. In this section, we are going to explain the calculation setting.

5.4.1. Boundary condition

In this calculation, the slip condition is applied to the surrounding wall which is same as previous diffuser calculation. Also, the inlet condition and outlet condition are the same. The most critical factor in this calculation is the condition at the boundary between the rotating region and the stable region. In this case, the boundary condition called CyclicAMI in OpenFOAM was used since the adjacent patch has the same shape but the relative positional relationship of cells changes. AMI means Arbitrary Mesh Interface, and we can connect both by specifying cyclic AMI and boundary conditions. This can be set with constant > polymesh > boundary. The setting contents are shown below. It is also necessary to specify the name of the adjacent patch in the neighbourPatch part along with the boundary condition. In this calculation, we name the rotating area side as AMI 1 and the stable area side as AMI 2.

```
AMI2
{
    type            cyclicAMI;
    neighbourPatch AMI1;
    nFaces          2292;
    startFace       4965691;
}
AMI1
{
    type            cyclicAMI;
    neighbourPatch AMI2;
    nFaces          36286;
    startFace       4967983;
```

5.4.2. Initial value

Inlet flow velocity, turbulent k, and turbulent omega are shown on Table.5-4.
In this calculation, an initial flow velocity is given to the fluid, and at the same time, an angular velocity is given to the turbine to make the same situation as in power generation. Since the tip speed ratio of the used turbine is 4.0, the following Eq. (5-1) is used to calculate the angular velocity. Here, λ is the tip speed ratio, ω is the angular velocity [rad / s], and R is the turbine radius. For V_∞, since the average velocity inside the diffuser ratio of the slim model at the flow velocity of 9 [m / s] was 1.58 from this study, 14.22 [m / s] was used as Flow velocity passing near the turbine.

$$\lambda \, V_\infty = \omega \, R \qquad\qquad (5\text{-}1)$$

The calculated 230 [rad / s] was set as the angular velocity, and it was set by constant▷ dynamicMeshDict. Even we set the axis for rotation in this file. The actual contents are shown below.

```
cellZone        rotor;

solidBodyMotionFunction  rotatingMotion;
rotatingMotionCoeffs
{
```

```
        origin     (0 0 0);
        axis       (0 0 1);
        omega      230; // rad/s
    }
}
```

Table. 5-4 Initial value

The flow velocity for this calculation [m/s]	9.0
turbulent k [m²/s²]	0.30
turbulent omega [s⁻¹]	2,745,013.374
Re	1.61×10^6

5.4.3. Time step

In unsteady flow analysis, the calculation is performed by dividing the whole calculation into a short time and repeating the task of calculating the phenomenon at the next moment from the state at a specific moment. Since the process of the phenomenon has a physical meaning and you can see how the change to the final state is. The time from this moment to the next moment is called the time step. When analyzing for a certain period, the number of iterations can be reduced as the value of the time step is increased, so that the calculation can proceed at high speed, but the accuracy of the prediction decreases by that amount. Therefore, it is essential to set an appropriate time interval in transient analysis. Timestep of this calculation used the function of OpenFOAM, adjustableRunTime. This is a function to automatically adjust timestep so that it does not exceed the maximum Courant number. It is desirable that Courant number should be 1 or less in all meshes, but the maximum Courant number was set to 1.5 in consideration of the variation in the size of the mesh and the calculation time. Here is the system> controldict that set it up.

```
application     pimpleDyMFoam;

startFrom       latestTime;

startTime       0;

stopAt          endTime;

deltaT          1e-5;
writeControl    adjustableRunTime;
writeInterval   0.001;

runTimeModifiable true;

adjustTimeStep  yes;

maxCo           1.5;
```

5.4.4. Test for rotating mesh

Before the main calculation, calculation for rotation without inflow was carried out as a test. We used the same mesh as the main calculation and gave an angular velocity of 140 [rad/s]. The other conditions are the same as this main calculation. Calculation up to 0.3 seconds was done for the convenience of time. Fig. 5-4 shows the results of streamlines every 0.1 second. Since there is no inflow, the flow is circulating. We decided to perform the main calculation using this mesh.
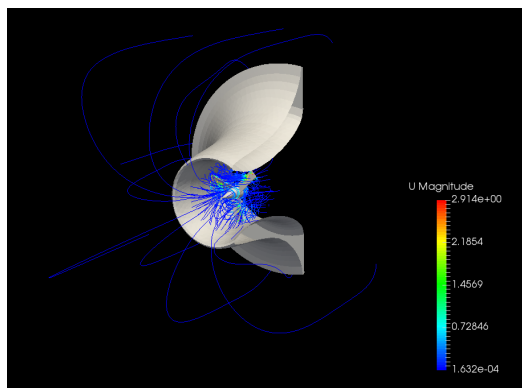
Fig. 5-4 (a) The result of the test at 0.1 [s]
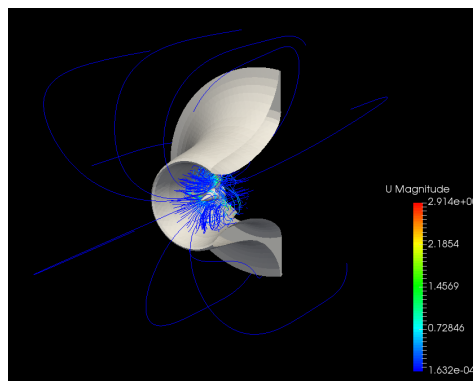
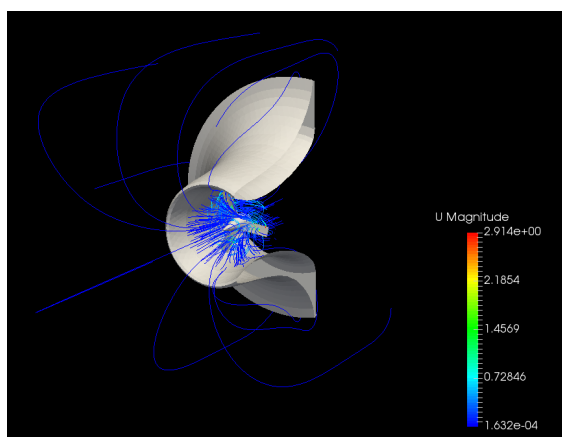Fig. 5-4 (b) The result of the test at 0.2 [s]

Fig. 5-4 (c) The result of the test at 0.3 [s]

5.5. Results and discussion

In this section, results of this calculation are shown and discussed. We compare the influence of the rotation of the turbine on the wake flow with the calculation result by comparing with the result of only the diffuser case shown in Chapter 4. As an example of the result, Fig. 5-5 shows the results of magnitude of velocity at 0.03 [s], 0.06 [s], 0.09 [s], 0.12 [s]. The flow velocity inside the diffuser is increased by the effect of the wind lens technology. In the behind the turbine, a velocity change with time can be seen. The turbulence of this flow is one which was not confirmed in the calculation of diffuser alone. Furthermore, we consider the horizontal flow velocity, vorticity and pressure distribution.
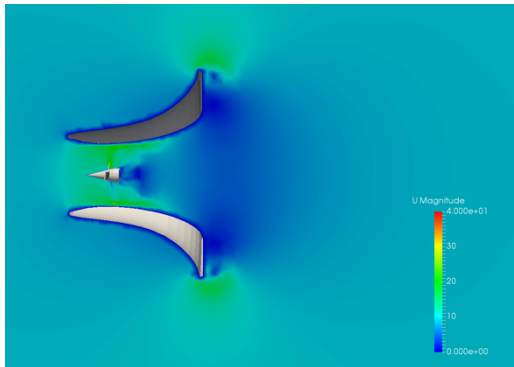

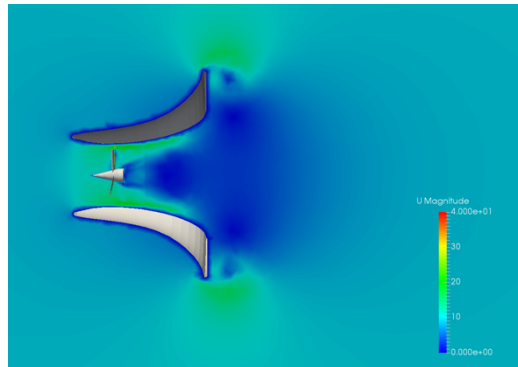Fig. 5-5 (a) Magnitude of velocity at 0.03 [s]
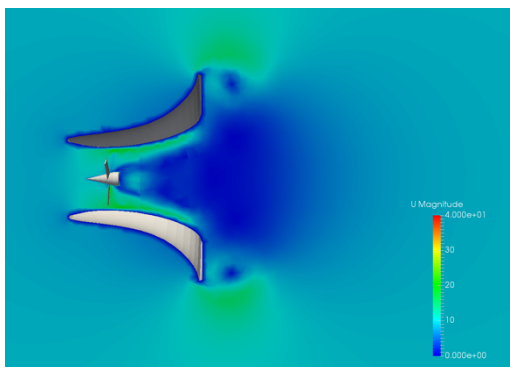

Fig. 5-5 (b) Magnitude of velocity at 0.06 [s]
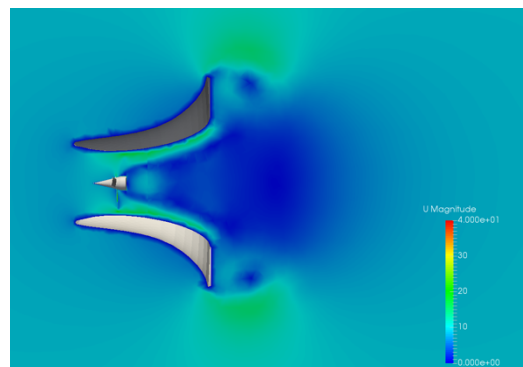

Fig. 5-5 (c) Magnitude of velocity at 0.09 [s]

Fig. 5-5 (d) Magnitude of velocity at 0.12 [s]

5.5.1. Horizontal flow velocity

In this section, we consider the flow velocity in the horizontal direction. Fig. 5-6 shows the results of horizontal flow velocity at 0.03 [s], 0.06 [s], 0.09 [s], 0.12 [s].

The flow velocity before the turbine does not change, but the flow behind the turbine has a different horizontal flow velocity distribution depending on the time by the rotation. The region with the negative velocity behind the turbine confirmed and got larger as time passes. This region that could not be confirmed by calculation of only the diffuser case.

In order to research the flow field deeper in the future, it is necessary to take long calculation time and observe the flow field.
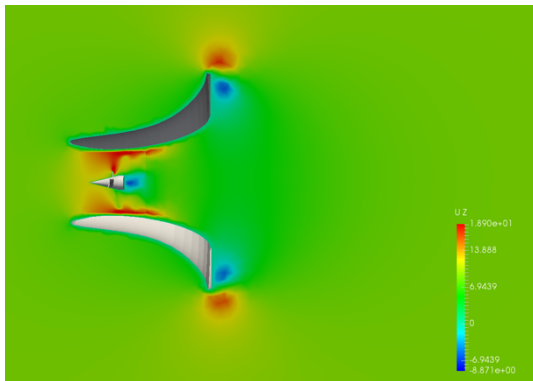

Fig. 5-6 (a) Horizontal flow velocity
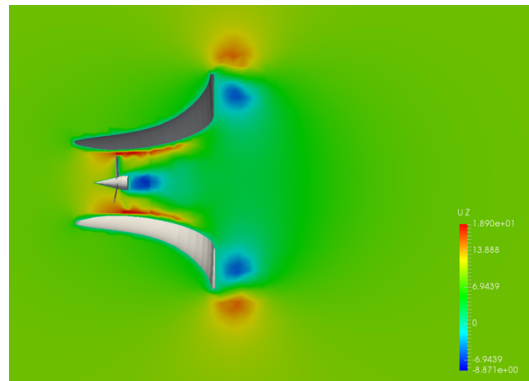at 0.03 [s]

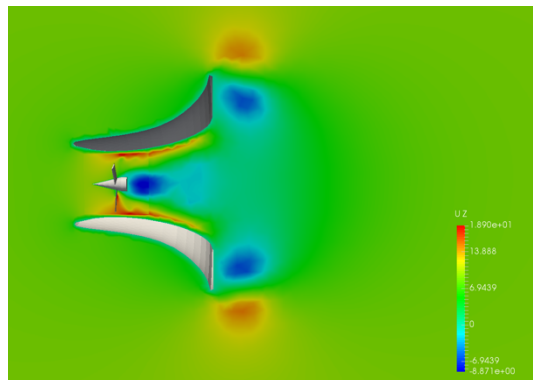

Fig. 5-6 (b) Horizontal flow velocity
at 0.06 [s]

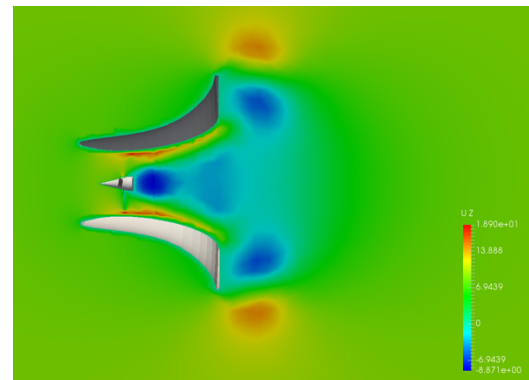Fig. 5-6 (c) Horizontal flow velocity
at 0.09 [s]

Fig. 5-6 (d) Horizontal flow velocity
at 0.12 [s]

5.5.2. Vorticity

Fig. 5-7 shows the results of vorticity magnitude. Vortex formed behind the diffuser by the diffuser and the brim. It can also be confirmed that a small vortex formed inside the diffuser by the rotation of the turbine. This point is great difference from the only the diffuser case. Changes in the vorticity inside the diffuser influence the wake behind. Moreover, the deformation of the wake can affect the performance of the diffuser. Therefore, it is necessary to study with the model considering the rotation of the turbine.
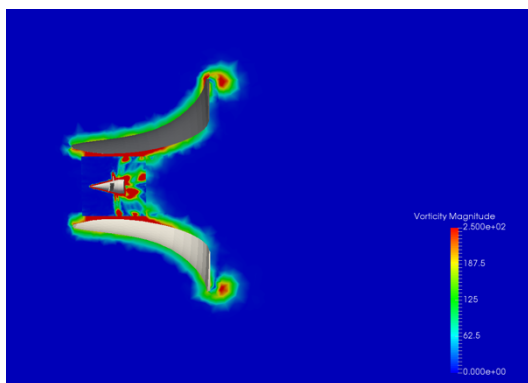

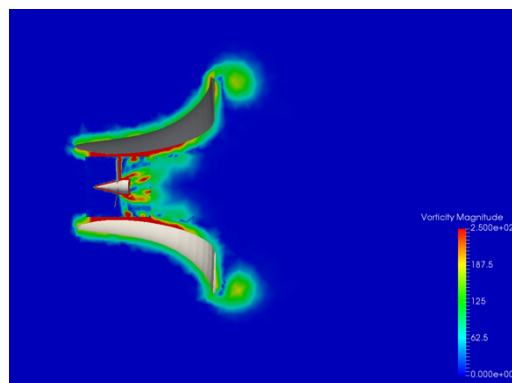Fig. 5-7 (a) Vorticity magnitude
at 0.03 [s]

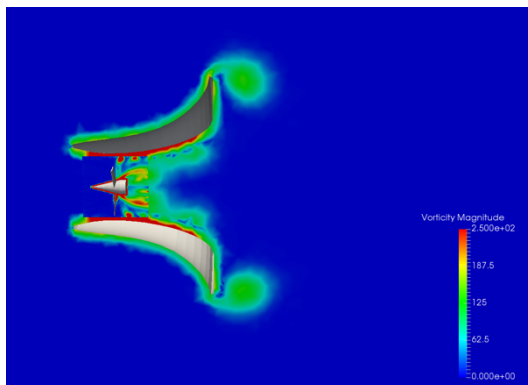Fig. 5-7 (b) Vorticity magnitude
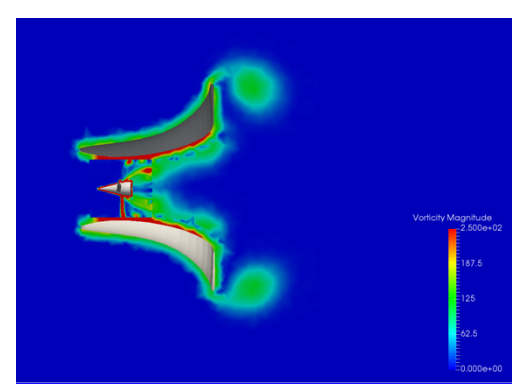at 0.06 [s]

Fig. 5-7 (c) Vorticity magnitude
at 0.09 [s]

Fig. 5-7 (d) Vorticity magnitude
at 0.012 [s]

Chapter 6: Conclusions

In this study, as a continuation of the previous research, an optimization investigation of the diffuser shape has been carried out. Especially, the influence of the diffuser thickness on the flow velocity increase inside the diffuser and the drag force on the diffuser, is studied by using CFD simulation. The open source code OpenFOAM is used for the numerical simulation. Three diffuser models with different thickness are considered. Numerical simulations are performed on the three diffuser models without turbine under different inflow velocities. A summary of the research achievements is described as follows.

● When the diffuser is thin with the brim standing at an angle close to perpendicular to the flow, the low-pressure area behind the diffuser becomes larger and the velocity inside the diffuser increases. This is the principle of the wind lens technology, which has been successfully applied in wind turbine developments. In this study we also applied it to the tidal current turbine system to increase the energy converter efficiency.

● There are many parameters that can affect the efficiency of the diffuser. Generally, when the flow acceleration inside the diffuser is enhanced by changing diffuser parameters, the drag force acting on the diffuser is often increased as a result. High drag force will result in high mooring cost, which is not recommended. Therefore, such problem is needed to consider in the design of the diffuser. In this study, the diffuser thickness is investigated because it is considered as one of the most important parameters.

● Through the numerical simulation on the three diffuser models with different thickness, it is shown that when the diffuser thickness increases, the strength of the vortex formed behind the diffuser is reduced, and the drag force also becomes small. On the other hand, diffuser thickness increase will reduce the flow acceleration inside the diffuser.

● A quantitative analysis of the relation between the thickness of the diffuser and the flow acceleration as well as the relation between the thickness of the diffuser and the drag force has been performed. Discussions have been provided on how to improve the design of the new tidal turbine system by using the information obtained from the numerical simulations.

● The numerical implementation by using OpenFOAM on simulation of rotating turbine inside a thin diffuser has been completed. A preliminary test calculation has been carried out and reasonable numerical has been obtained. Numerical simulation of a rotating turbine with a diffuser requires much more meshes and time, and is left for future research.

References

[1] United nations. World Population Prospects 2017 [DB/OL].

[2] International Energy Agency. World Energy Outlook 2017 [DB/OL]. [2017-11-14]

[3] New Energy and Industrial Technology Development Organization (NEDO)
「NEDO 再生可能エネルギー技術白書 第 2 版」[M].
New Energy and Industrial Technology Development Organization, 2014

[4] Ministry of Economy, Trade and Industry, Agency for Natural Resources and Energy
「平成 27 年度エネルギーに関する年次報告」[M]

[5] International Energy Agency. World Energy Outlook 2011 [DB/OL]. [2011-11-9]

[6] International Energy Agency. World Energy Outlook 2012 [DB/OL]. [2012-11-23]

[7] United Nations Environment Programme, UNEP 2007 ANNUAL REPORT [M],
United Nations Environment Programme, 2008

[8] United Nations Development Programme, HUMAN DEVELOPMENT REPORT 2001 [M],
New York : Oxford University Press, 2001

[9] Japan Coast Guard, Japan Coast Guard Justice and Humanity [M],
Japan Coast Guard, 2018

[10] Zaikei News,
川崎重工、海洋エネルギーを利用した「潮流発電システム」の開発に着手 [N],
Zailei News, 2011.

[11] 第二回浮沈式発電装置研究会 発表資料 [Z], 2017

[12] Yuji Ohya. *Wind lens technology and its application to wind and water turbine and beyond*
[J], Renewable Energy and Environmental Sustainability, 2017, Vol. 2.

[13] Yuji Ohya, Takashi Karasudani.
A Shrouded Wind Turbine Generating High Output Power with Wind-lens Technology [J],
Energies, 2010, Vol. 3, 634-649.

[14] Yuji Ohya, Takashi Karasudani and Akira Sakurai. *Development of High-Performance Wind
Turbine with Brimmed Diffuser* [J], 日本航空宇宙学会論文集, Vol. 50, No. 587, 2002, 477–
482.

[15] Minoru Nagai and Kunio Irabu. *Momentum Theory of Diffuser Augmented Wind Turbine* [J]
日本機械学会論文集, Vol. 53, 1987, 1543-1547

[16] Takashi Karasudani, Yuji Ohya, Nobutaka Fukamachi and Kimihiko Watanabe. *Wind-Velocity
Acceleration by Hollow Bodies* [J], 日本流体力学会誌「ながれ」, Vol. 22, 2003, 477–482.

[17] Kento Obara. 新型浮沈式潮流発電における成立性に関する基礎的研究 [D]. Fukuoka :
Kyushu University, 2017.

[18] Rhinoceros modeling tool for designers ［DB/OL］ [2018-12-18] https://www.rhino3d.co.jp/

[19] The Open Acoustics Team, Gmsh クイックスタート・ガイド [M],
The Open Acoustics Team, 2010

[20] Salome-platform [DB/OL]. [2018-12-18] https://www.salome-platform.org/

[21] OpenCAE Users Wiki [DB/OL]. [2018-12-18]
http://opencae.gifunct.ac.jp/pukiwiki/index.php

[22] OpenFOAM [DB/OL]. [2018-12-18] https://www.openfoam.com/

[23] The OpenFOAM Foundation [DB/OL]. [2018-12-18] https://openfoam.org/

[24] Kazunari Tanaka, Yuji Ohya, Takashi Karasudani, Kimihiko Watanabe. *Wind Resistant
Performance Test of Wind Lens Turbines* [J], 風力エネルギー利用シンポジウム, Vol. 29,
2007, 292-295

[25] Yudai Shiraishi. 風レンズ用水車ブレードの開発 [D]. Fukuoka : Kyushu University, 2011.

[26] Koki Akiyoshi. 潮流発電用タービンブレードの開発に関する研究 [D]. Fukuoka :
Kyushu University, 2015.

Acknowledgements

I would like to show my greatest appreciation to Prof. Changhong Hu, Assist. prof. Makoto Sueyoshi, Dr. Mohamed M. Kamra and the secretary Ms. Masako Yoshizu. They gave me constructive comments and warm encouragement to carry out my research and reach the completion of my Master's thesis.

I also would like to express my gratitude to emeritus Professor Yusaku Kyozuka (Organization for Marine Science and Technology of Nagasaki university). He gave me a lot of valuable advises to carry out this work.

And then, I would like to express my deepest thanks to my supervisor Assoc. Prof. Zhenyu Liu, not only for his kindness, but also his support throughout my stay in Shanghai Jiao Tong University. His support enabled me to spend a meaningful time in my university life.

Furthermore, I am very thankful to Prof. Seigi Mizuno, Prof. Byungkoog Jang, Prof. Tetsuo Tanabe, Assoc. Prof. Dong Wang, Ms. Nahoko Ichimura, and Ms. Kazuyo Nishiyama. They gave me the valuable opportunity to study in Shanghai Jiao Tong University and considerable supports to realize that.

I was able to carry out this research with the help of many other people. I cannot give all the names of those who took care of here, but I would like to express my thanks to you.

Finally, lots of thanks are given to my parents and sisters.
Without their mentally and economically support, I cannot fulfill this work.

<div align="right">Koichiro Urakawa</div>